

Tinker-*HP* : Accelerating Molecular Dynamics Simulations of Large Complex Systems with Advanced Point Dipole Polarizable Force Fields using GPUs and Multi-GPUs systems

Olivier Adjoua,[†] Louis Lagardère^{*,‡,‡} Luc-Henri Jolly,[‡] Arnaud Durocher,[¶] Thibaut Very,[§] Isabelle Dupays,[§] Zhi Wang,^{||} Théo Jaffrelot Inizan,[†] Frédéric Célerse,^{†,⊥} Pengyu Ren,[#] Jay W. Ponder,^{||} and Jean-Philip Piquemal^{*,†,#}

[†]*Sorbonne Université, LCT, UMR 7616 CNRS, F-75005, Paris, France*

[‡]*Sorbonne Université, IP2CT, FR2622 CNRS, F-75005, Paris, France*

[¶]*Eolen, 37-39 Rue Boissière, 75116 Paris, France*

[§]*IDRIS, CNRS, Orsay, France*

^{||}*Department of Chemistry, Washington University in Saint Louis, USA*

[⊥]*Sorbonne Université, CNRS, IPCM, Paris, France.*

[#]*Department of Biomedical Engineering, The University of Texas at Austin, USA*

E-mail: louis.lagardere@sorbonne-universite.fr, jean-philip.piquemal@sorbonne-universite.fr

Abstract

We present the extension of the Tinker-*HP* package (Lagardère et al., *Chem. Sci.*, 2018, 9, 956-972) to the use of Graphics Processing Unit (*GPU*) cards to accelerate molecular dynamics simulations using polarizable many-body force fields. The new high-performance module allows for an efficient use of single- and multi-*GPUs* archi-

tectures ranging from research laboratories to modern supercomputer centers. After detailing an analysis of our general scalable strategy that relies on OPENACC and CUDA , we discuss the various capabilities of the package. Among them, the multi-precision possibilities of the code are discussed. If an efficient double precision implementation is provided to preserve the possibility of fast reference computations, we show that a lower precision arithmetic is preferred providing a similar accuracy for molecular dynamics while exhibiting superior performances. As Tinker-*HP* is mainly dedicated to accelerate simulations using new generation point dipole polarizable force field, we focus our study on the implementation of the AMOEBA model and provide illustrative benchmarks of the code for single- and multi-cards simulations on large biosystems encompassing up to millions of atoms. The new code strongly reduces time to solution and offers the best performances ever obtained using the AMOEBA polarizable force field. Perspectives toward the strong-scaling performance of our multi-node massive parallelization strategy, unsupervised adaptive sampling and large scale applicability of the Tinker-*HP* code in biophysics are discussed. The present software has been released in phase advance on GitHub in link with the High Performance Computing community COVID-19 research efforts and is free for Academics (see <https://github.com/TinkerTools/tinker-hp>).

Introduction

Molecular dynamics (MD) is a very active research field that is continuously progressing.^{1,2} Among the various evolutions of the field, the definition of force fields themselves grows more complex. Indeed, beyond the popular pairwise additive models³⁻⁷ that remain extensively used, polarizable force field (PFF) approaches are becoming increasingly mainstream and start to be more widely adopted,⁸⁻¹¹ mainly because accounting for polarizability is often crucial for complex applications and adding new physics to the model through the use of many-body potentials can lead to significant accuracy enhancements.¹⁰ Numerous approaches are currently under development but a few methodologies such as the Drude¹²⁻¹⁴

or the AMOEBA^{15–17} models emerge. These models are more and more employed because of the alleviation of the main bottleneck of these methods: their larger computational cost compared to classical pairwise models. Indeed, the availability of High Performance Computing (HPC) implementations of such models within popular packages such as NAMD¹⁸ or GROMACS¹⁹ for Drude or Tinker-*HP*²⁰ for AMOEBA fosters the diffusion of these new generation techniques within the research community. This paper is dedicated to the evolution of the Tinker-*HP* package.²⁰ The software, which is part of the Tinker distribution,²¹ was initially introduced as a double precision massively parallel MPI addition to Tinker dedicated to the acceleration of the various PFFs and non-polarizable force fields (n-PFFs) present within the Tinker package. The code was shown to be really efficient, being able to scale on up to tens of thousand cores on modern petascale supercomputers.^{20,22} Over the years, it has been optimized on various platforms taking advantage of vectorization and of the evolution of the recent *CPUs* (Central Processing Units).²² However, in the last 15 years, the field has been increasingly using *GPUs* (Graphic Processor Unit)^{23–25} taking advantage of low precision arithmetic. Indeed, such platforms offer important computing capabilities at both low cost and high energy efficiency allowing for reaching routine microsecond simulations on standard *GPUs* cards with pair potentials.^{24,26} Regarding the AMOEBA polarizable force field, the OpenMM package²⁷ was the first to propose an AMOEBA-GPU library that was extensively used within Tinker through a specific implementation that could be used in Tinker using the Tinker-OpenMM *GPU* interface.²⁸ The present contribution aims to address two goals: i) the design of an efficient native Tinker-*HP* GPU implementation; ii) the HPC optimization in a massively parallel context to address both the use of research laboratories clusters and modern multi-*GPUs* pre-exascale supercomputer systems. The paper is organized as follows. First, we will describe our OpenACC port and its efficiency in double precision. After observing the limitations of this implementation regarding the use of single precision, we introduce a new CUDA approach and detail the various parts of the code it concerns after a careful study of the precision. In both cases, we present benchmarks of the

new code on illustrative large biosystems of increasing size on various NVIDIA platforms (including 2080Ti, V100 and A100 cards). Then, we explore how to run on even larger systems and optimize memory management by making use of latest tools such as NVSHMEM.²⁹

OPENACC Approach

Global overview and definitions

Tinker-*HP* is a molecular dynamics application with a MPI layer allowing a significant acceleration on *CPUs*. The core of the application is based on the resolution of the classical newton equations^{30,31} given an interaction potential (force field) between atoms. In practice, a molecular dynamic simulation consists into the repetition of the call to an integrator routine defining the changes of the positions and the velocities of all the atoms of the simulated system between two consecutive time steps. The same process is repeated as many times as needed until the simulation duration is reached (see Figure 3). To distribute computations over the processes, a traditional three dimensional domain decomposition is performed on the simulation box (Ω) which means that it is divided in subdomains (ψ), each of which being associated to a MPI process. Then, at each time step, positions of the atoms and forces are exchanged between processes before and after the computation of the forces. Additionally, small communications are required after the update of the positions to deal with the fact that an atom can change of subdomain during a time step. This workflow is described in detail in reference.³¹

In recent years a new paradigm has emerged to facilitate computation and programming on GPU devices. In the rest of the text, we will denote as *kernel* the smallest piece of code made of instructions designed for a unique purpose. Therefore a succession of kernels might constitute a *routine*. Then a *program* can be seen as a collection of routines, each of them representing an essential component of an application. There are two types of kernels

- *Serial* kernel, mostly used for variable configuration

- *Loops* kernel, operating on multiple data sets

This approach, called OPENACC ^{,32,33} is a directive-based language close to the multi-threading OpenMP paradigm with an additional complexity level. Since a target kernel is destined to be executed on *GPUs* , it becomes crucial to manage data between *GPUs* and *CPUs* . At the most elementary level, OPENACC interacts on a standard host (CPU) kernel and generates a device (GPU) kernel using directives implemented to describe its parallelism along with clauses to manage global data behaviour at both entry and exit point and/or kernel launch configuration [Figure 1]. This method offers two majors benefits. Unlike the low-level CUDA programming language,³⁴ it takes only a few directives to generate a device kernel. Secondly, the same kernel is compatible with both platforms -*CPUs* and *GPUs* -. The portability along with all the associated benefits such as host debug is therefore ensured. However, there are some immediate drawbacks mainly because *CPUs* and *GPUs* do not share the same architecture and specifications. While *CPUs* are optimized for serial tasks, a full GPU compute potential can only be reached with parallel tasks. This requires a parallelism property on most device kernels. As a direct consequence, it may be necessary to reshape kernels to fit device architecture in order to get appropriate acceleration. Once we clearly exhibit a kernel parallelism and associate OPENACC directives to offload it on device, it should perform as well as if it had been in native CUDA. Still, in addition to kernel launch instruction (performed by both OPENACC and CUDA) before the appropriate execution, there is a global data checking operation overhead which might slow down execution [Figure 1]. However, this operation can be overlapped using asynchronous device streams in the kernel configuration [Figure 2]. It is safe to assume that under proper conditions, there should not be any major performance difference between both OPENACC and CUDA.

In the following, we will say that a kernel is *semi-parallel* if one can find a partition inside the instructions sequence which does not share any dependency at all. A semi-parallel kernel is consequently defined *parallel* if all instructions in the partition do not induce a race condition within its throughput.

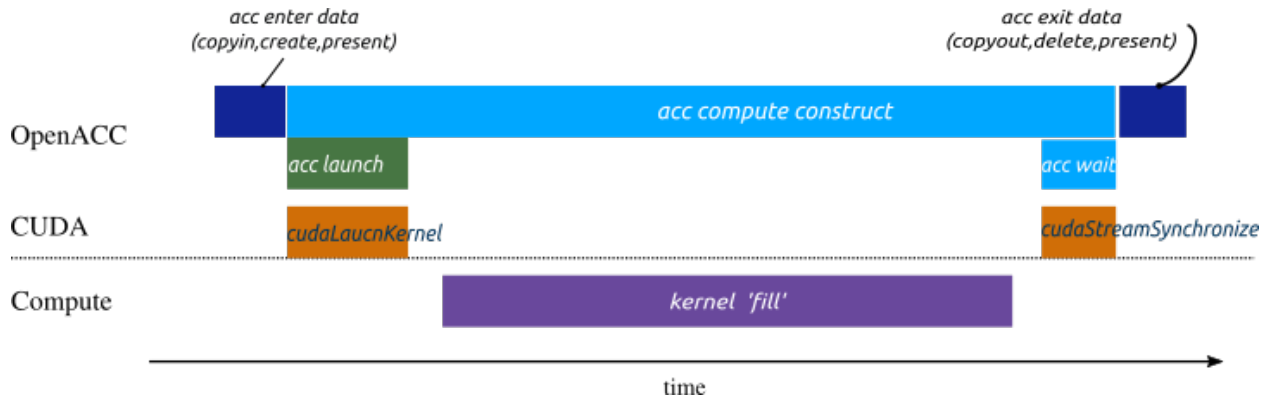


Figure 1: OPENACC synchronous execution model on test kernel <fill>

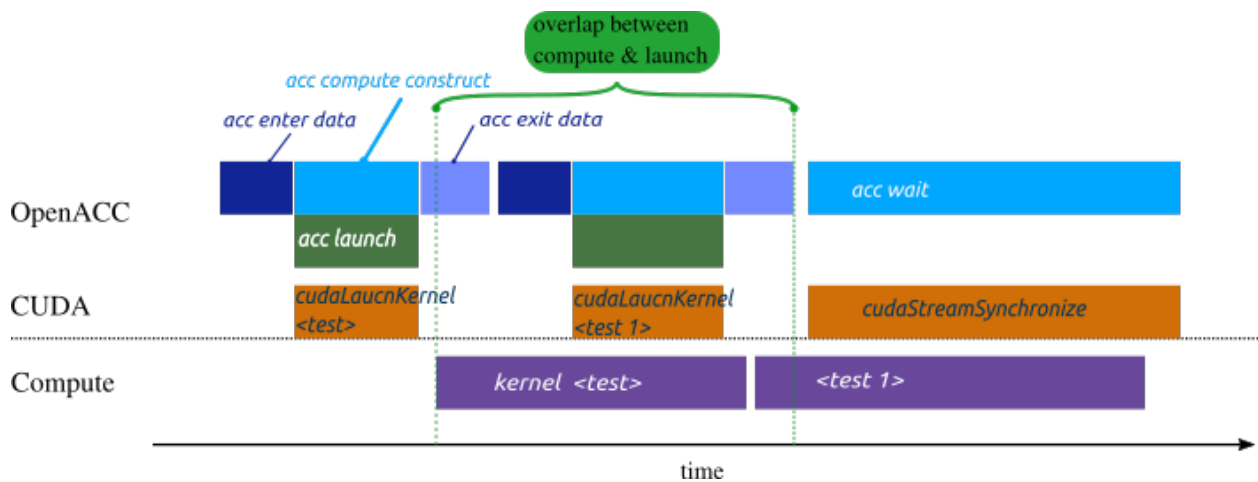


Figure 2: OPENACC asynchronous execution on both kernels <test> & <test 1>.

Once a kernel is device compiled, his execution requires a configuration which define the resources provided by the device to perform on it. With OPENACC , those resources are respectively the total number of threads and the assignment stream. We can access the first one through the *gang* and *vector* clauses attached to a device compute region directive. A **gang** is a collection of vectors inside of which every thread can share cache memory. All gangs run separately on device streaming multi-processors (SM) to process kernel instructions inside a stream where many other kernels are sequentially queued. OPENACC offers an intermediate parallelism level between **gang** and **vector** called **worker** . This level can be seen as a gang subdivision.

It is commonly known that *GPUs* are inefficient for sequential execution due to their latency. To cover up latency, each SM comes with a huge register file and cache memory in order to hold and run as many vectors as possible at the same time. Instructions from different gangs are therefore pipe-lined and injected in the compute unit.^{34,35} From this emerges the kernel occupancy's concept which is defined as the ratio between the gang's number concurrently running on one SM and the maximum gang number that can actually be held by this SM.

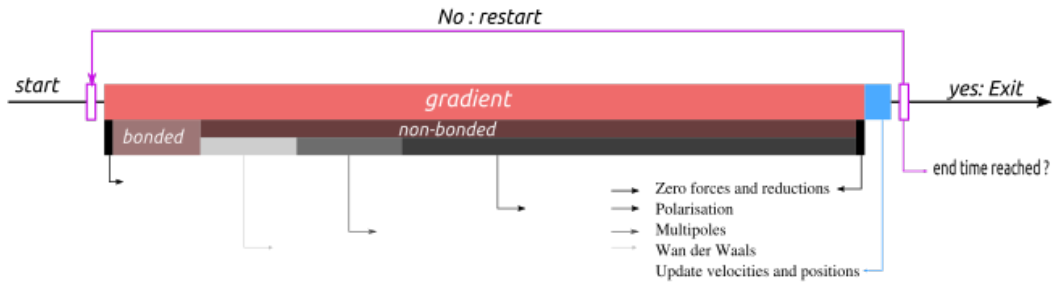


Figure 3: Integrator algorithm performance visualization

Global scheme

The *parallel* computing power of *GPUs* is in constant evolution and the number of streaming multiprocessors (SM) is almost doubling with every generation unlike traditional *CPUs* .

Considering their impressive compute potential in comparison to CPUs, it becomes safe to assume that the only way to fully benefit from this power is by offloading the entire application on device. Any substantial part of the workflow of Tinker-*HP* should not be performed on the CPU platform. It will otherwise represent a bottleneck to performance in addition to requiring multiple data transfers. As for all MD applications, most of the computation lies in the evaluation of the forces. For the AMOEBA polarizable model, it takes around 97% of a time step to evaluate those forces when running sequentially on CPU platform. Of these 97%, around 10% concern bonded forces and 90% the non bonded ones, namely: polarization, (multipolar) permanent electrostatics and van der Waals. The polarization which includes the iterative resolution of induced dipoles largely dominates this part (see [Figure 3]). Non-bonded forces and polarization in particular will thus be our main focus regarding the porting and optimization. We will then benefit from the already present Tinker-*HP* MPI layer^{20,22} to operate on several *GPUs*. The communications can then be made directly between *GPUs* by using a CUDA aware MPI implementation.³⁶ The Smooth Particle Mesh Ewald method^{31,37,38} is at the heart of both the permanent electrostatics and polarization non-bonded forces used in Tinker-*HP*, first through the iterative solution of the induced dipoles and then through the final force evaluation. It consists in separating the electrostatic energy in two independent pieces: real space contribution and reciprocal space contribution. Let us describe our OPENACC strategy regarding those two terms.

Real space scheme

Because the real space part of the total PME energy and forces has the same structure as the van der Waals one, the associated OPENACC strategy is the same. Evaluating real space energy and forces is made through the computation of pairwise interactions. Considering n atoms, a total of $n(n-1)$ pairwise interactions need to be computed. This number is reduced by half because of the symmetry of the interactions. Besides, because we use a cutoff distance after which we neglect these interactions, we can reduce their number to being proportional

to n in homogeneous systems by using neighbor lists. The up-bound constant is naturally reduced to a maximum neighbors for every atoms noted as Neig_{max} .

The number of interactions is up-bounded by $n * \text{Neig}_{max}$. In terms of implementation, we have written the compute algorithm into a single loop kernel. As all the interactions are independent, the kernel is semi-parallel. By making sure that energy and forces are added one at a time, the kernel becomes parallel. To do that, we can use atomic operations on *GPUs* which allow to make this operation in parallel and solve any race condition issue without substantially impacting parallel performance. By doing so, real space kernels looks like [Listing 1]

```

c$acc parallel loop gang default(present) async
c$acc&      private(scaling_data)
do i = 1,numLocalAtoms
  iglob = glob(i) ! Get Atom i global id
  !Get Atom iglob parameter and positions
  ...
  !Gather Atoms iglob scaling interactions in 'scaling_data'
  ...
c$acc loop vector
  do k = 1, numNeig(i)
    kglob = glob( list(k,i) )
    ! Get Atom kglob parameter and positions
    ! Compute distance (d) between iglob & kglob
    if (d < dcut) then
      call resolve_scaling_factor(scaling_data)
      ...
      call Compute_interaction !inlined
      ...
      call Update_(energy,forces,virial)
    end if
  end do

```

```
end do
```

Listing 1: OPENACC real space offload scheme. The kernel is offloaded on device using two of the three parallelism levels offered by OPENACC . The first loop is broken down over gangs and gathers all data related to atom `oglob` using gang’s shared memory through the private clause. OPENACC vectors are responsible of the evaluation and the addition of forces and energy after resolving scaling factor if necessary. Regarding data management we make sure with the present clause that everything is available on device before the execution of the kernel.

At first, our approach was designed to directly offload the CPU vectorized real space compute kernels which use small arrays to compute pairwise interactions in hope to align memory access pattern at the vector level and therefore accelerate the code.²² This requires each gang to privatize every temporary array and results in a significant overhead with memory reservation associated to a superior bound on the gang’s number. Making interactions computation scalar helps us remove those constraints and double the kernel performance. The explanation behind this increase arises from the use of GPU scalar registers. Still, one has to compute the scaling factors of the interactions. As it happens inside gang shared memory, the performance is lightly affected. However, we would benefit from a complete removal of this inside search. Two drawbacks are to be listed.

- > Scaling interactions between neighboring atoms of the same molecule can become very complex. This is particularly true with large proteins. Storage workspace can potentially affect shared memory and also kernel’s occupancy.
- > Depending on the interactions, there is more than one kind of scaling factor. For example, every AMOEBA polarization interaction needs three different scaling factors.

The best approach is then to compute scaling interactions separately in a second kernel. Because they only involve connected atoms, their number is small compared to the total number of non-bonded interactions. We first compute unscaled non-bonded interactions and

then apply scaling correction in a second part. An additional issue is to make this approach compatible with the 3d domain decomposition. Our previous kernel then reads: 2.

```
c$acc parallel loop gang default(present) async
do i = 1,numLocalAtoms
    iglob = glob(i) ! Get Atom i global id
    !Get Atom iglob parameter and positions
    ...
c$acc loop vector
do k = 1, numNeig(i)
    kglob = glob( list(k,i) )
    ! Get Atom kglob parameter and positions
    ! Compute distance (d) between iglob & kglob
    if (d < dcut) then
        call Compute_interaction !inlined
        ...
        call Update_(energy,forces,virial)
    end if
end do
end do

call correct_scaling
```

Listing 2: final OPENACC real space offload scheme. This kernel is more balanced and exposes much more computational load over vectors. 'correct_scaling' routine applies the scaling factors. This procedure is much more suitable to device execution.

Reciprocal space scheme

The calculation of Reciprocal space PME interactions essentially consists in five steps:

1. Interpolating the (multipolar) density of charge at stake on a 3D grid
2. Switching to Fourier space by using a forward fast Fourier transform (FFt)
3. Performing a trivial scalar product in reciprocal space
4. Performing a backward FFt to switch back to real space

5. Performing a final multiplication by b-splines to interpolate the reciprocal forces

Regarding parallelism, Tinker-*HP* uses a two dimensional decomposition of the associated 3d grid based on successive 1D FFT's. Here, we use the cuFFT library.³⁹ The OPENACC offload scheme for reciprocal space is described in [Figure 4]



Figure 4: Reciprocal space offload scheme. Charge interpolation and Force interpolation are both written in a single kernel. They are naturally parallel except for the atomic contributions to the grid in the first one. The approach remains the same for data management between host and device as for real space: all data are by default device resident to prevent any sort of useless transfer. Regarding MPI communications, exchanges take place directly between GPUs through interconnection.

We just reviewed our offload strategy of the non-bonded forces kernels with OPENACC, but the bonded ones remain to be treated. Also, the MPI layer has to be dealt with. The way bonded forces are computed is very similar to the real space ones, albeit simpler, which makes their offloading relatively straightforward. MPI layer kernels require, on the other hand, a slight rewriting as communications are made after a packing pre-treatment. In parallel, one does not control the throughput order of this packing operation. This is why it becomes necessary to also communicate the atom list of each process to their neighbors. Now that we presented the main offload strategies, we can focus on some global optimizations regarding the implementation and execution for single and multi-*GPUs*. We were able to identify and apply several optimizations during our work. Some of them lead to very different results depending on the device architecture.

Optimizations opportunities

> A first optimization is to impose an optimal bound on the **vector** size when computing pair interactions. In a typical setup, for symmetry reasons, the number of neighbors for real space interactions vary between zero and a few hundreds. Because of that second

loop in [Listing 2], the smallest vector length (32) is appropriate to balance computation among the threads it contains. Another optimization concerns the construction of the neighbor lists. Let us remind that it consists in storing, for every atom, the neighbors that are closer than d_{cut} plus a d_{buff} . This buffer is related to the frequency at which the list has to be updated. To balance computation at the vector level and at the same time reduce warp discrepancy (as illustrated in [Figure 5]) we have implemented a reordering kernel: we reorder the neighbor list for each atom so that the firsts are the ones under d_{cut} distance.

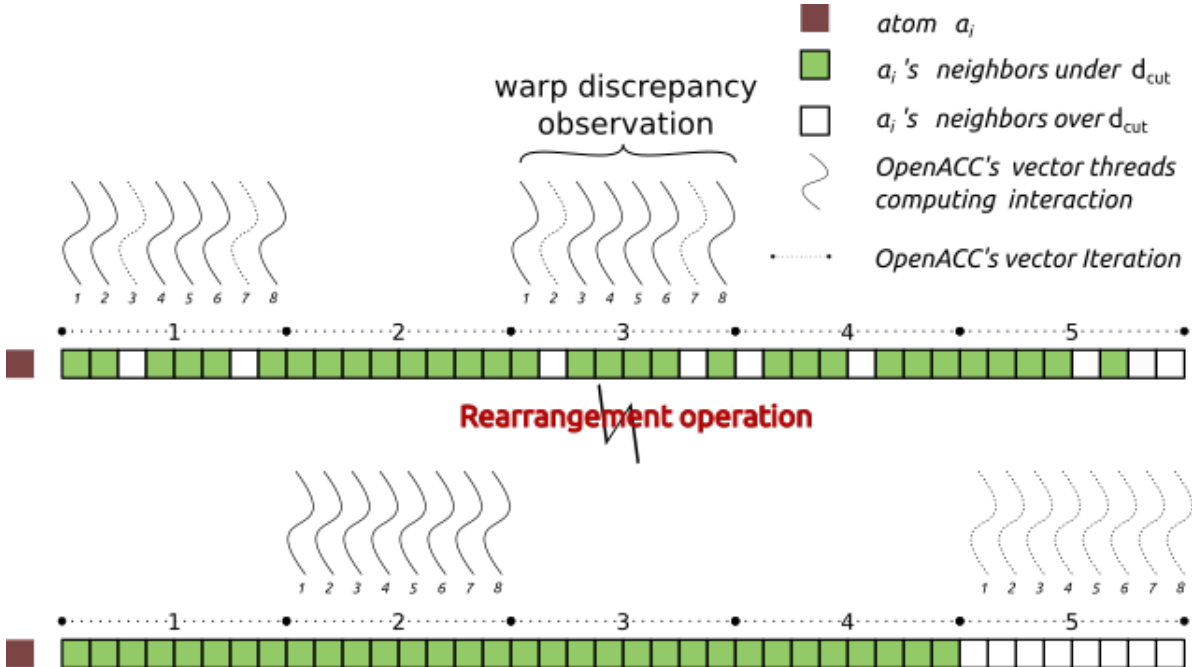


Figure 5: Illustration of compute balance due to the list reordering. Unbalanced computation in the first image induces an issue called warp discrepancy: a situation where all threads belonging to the same vector do not follow the same instructions. Minimizing that can increase kernel performance significantly since we ensure load balancing among each thread inside the vector.

> A second optimization concerns the iterative resolution of the induced dipoles. Among the algorithms presented in,^{38,40} the first method we offloaded is the preconditioned conjugated gradient (PCG). It involves a (polarization) matrix-vector product at each iteration. Here, the idea is to reduce the computation and favor coalesce memory access by precomputing and storing the elements of (the real space part) of the matrix before the iterations.

As the matrix-vector product is being repeated, we see a performance gain starting from the second iteration. But this method is memory consuming, and more suitable to host execution or a high level of multi device parallelism where the memory can be distributed.

- > An additional improvement concerns the two dimensional domain decomposition of the reciprocal space 3D grid involved with **FFt**. The parallel scheme for **FFt** used in Tinker-*HP* is the following for a forward transform:

$$FFT(s) \text{ 1d dim}(x) + x \text{ Transposition } y + FFT(s) \text{ 1d dim}(y) + y \text{ Transposition } z + FFT(s) \text{ 1d dim}(z) .$$

Each Transposition represents an all-to-all MPI communication which is the major bottleneck preventing most MD Applications using PME to scale across nodes.^{22,31,41} Given the *GPUs* huge compute power, this communication is even more problematic in that context. On device, we use the **cuFFt**³⁹ library. Using many **cuFFt** 1d batches is not as efficient as using less batches in a higher dimension. Indeed, devices are known to under perform with low saturation kernels. In order to reduce MPI exchanges and increase load on device, we adopted a simple 3d dimensional **cuFFt** batch when running on a single device. On multiple *GPUs*, we use the following scheme based on a 1d domain decomposition along the z axis :

$$cuFFt(s) \text{ 2d dim}(x,y) + y \text{ Transposition } z + cuFFt(s) \text{ 1d dim}(z)$$

which gives a 25% improvement compared to the initial approach.

- > Profiling the application on a single device, we observed that real space computation is on average 5 times slower than reciprocal space computation. This trend reverses using multiple *GPUs* because of the communications mentioned above. This motivated the assignment of these two parts in two different priority streams. The reciprocal kernels along with MPI communications are queued inside the higher priority stream, and real space kernels - devoid of communications - can operate at the same time on the lower priority stream to recover communications. This is illustrated in [Figure 6].

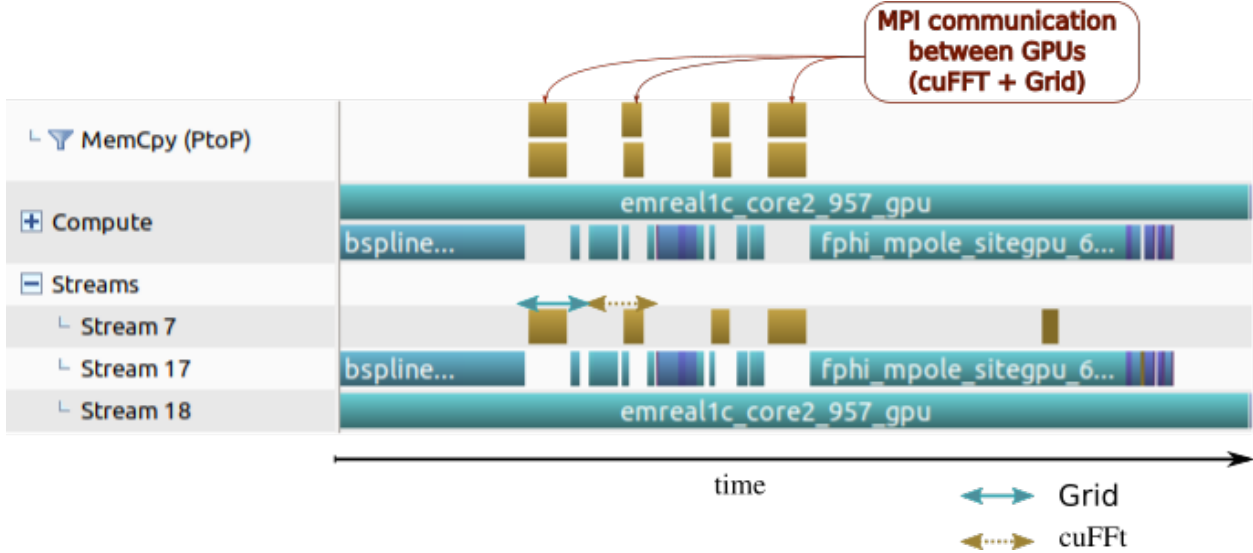


Figure 6: Representation of cuFFT’s communication recovering using device stream computation between direct and reciprocal space. Real space computation kernels are assigned to asynchronous stream 18. reciprocal ones goes into high priority asynchronous stream 17. real space kernel therefore recovers FFT grid exchanges. This profile was retrieved on 2 GPUs

Simulation Validation and Benchmarks

Here, we use the same bench systems as in reference.^{20,22} These are the solvated DHFR2 protein, along with the solvated COX protein and the STMV virus, all with the AMOEBA force field. They hold respectively 23 558, 171 219 and 1 066 600 atoms. The molecular dynamics simulations were run in the NVT ensemble at 300K for 5 pico-seconds simulation using a (bonded/non-bonded) RESPA integrator with a 2fs outer timestep (and a 1fs inner time step)⁴² and the Bussi thermostat.⁴³ For validation purposes, we compared the results of the first time step between Tinker-*HP* v1.2 release version and the GPU one. Note that we used here double precision DP on all platforms. Furthermore, we compared our results to a well known MD application: Tinker-OpenMM in the same exact setup.²⁸

We can directly observe the technical superiority of the Quadro architecture compared to the Geforce one. Double precision compute units of the V100 allow to vastly outperform the Geforce. In addition, by comparing the performance of the Geforce RTX to the one of the Quadro GV100, we see that Quadro devices are much less sensitive to warp discrepancy

Table 1: Single device benchmark : MD production per day (ns/day). All simulations were run using a RESPA/2 fs setup.

systems /devices (ns/day)	<i>CPUs</i> - one node	RTX 2080Ti	RTX 2080Ti + optim	V100	V100 + optim	Tinker- OpenMM V100
DHFR2	0.754	2.364	3.903	8.900	9.260	6.300
COX	0.103	0.341	0.563	1.051	1.120	0.957
STMV	0.013	n/a	n/a	0.111	0.126	0.130

and non-coalesce data accessing pattern. It is almost as if the architecture of the V100 card overcomes traditional optimizations techniques related to parallel device implementation. However, we see that our pure OPENACC implementation manages to deliver more performance than usual device MD application with polarizable force fields in DP . The V100 results were obtained on the Jean-Zay HPE SGI 8600 cluster of the IDRIS supercomputer Center (GENCI-CNRS, Orsay, France) which is made of 612 nodes, each of them made of 2 Intel Cascade Lake 6248 processors (20 cores at 2,5 GHz) accelerated with 4 NVIDIA Tesla V100 SXM2 *GPUs* with 32 Go of memory, interconnected through NVIDIA NVLink. Here as in all the tests presented in this paper, all the MPI communications were made with a CUDA aware MPI implementation.³⁶ This results is very satisfactory as a single V100 card is at least ten times faster than an entire node of this supercomputer using only CPUs.

Multi-device benchmark results compared with host-platform execution are presented in [Figure 7]. DHFR2 is to small to scale out. MPI communications overcomes the computations even with optimizations. On the other hand, COX and STMV show good multi-gpu performances. Adding our latest MPI optimizations - FFt reshaping and asynchronous compute between direct and reciprocal part of PME - allows an additional substantial gain in performances. We see that on a Jean-Zay node we can only benefit from the maximum communication bandwidth when running on the entire node, hence the relative inflexion point on the STMV performances on 2 *GPUs* . Indeed, all devices are interconnected inside one node in such a way that they all share interconnection bandwidth. More precisely, running on 2 *GPUs* reduces bandwidth by four and therefore affects the scalability. It is almost certain

that results would get better on an interconnected node made exclusively of 2 *GPUs* . Those results are more than encouraging considering the fact that we manage to achieve them with a full OPENACC implementation of Tinker-*HP* (direct portage of the reference CPU code) in addition to some adjustments.

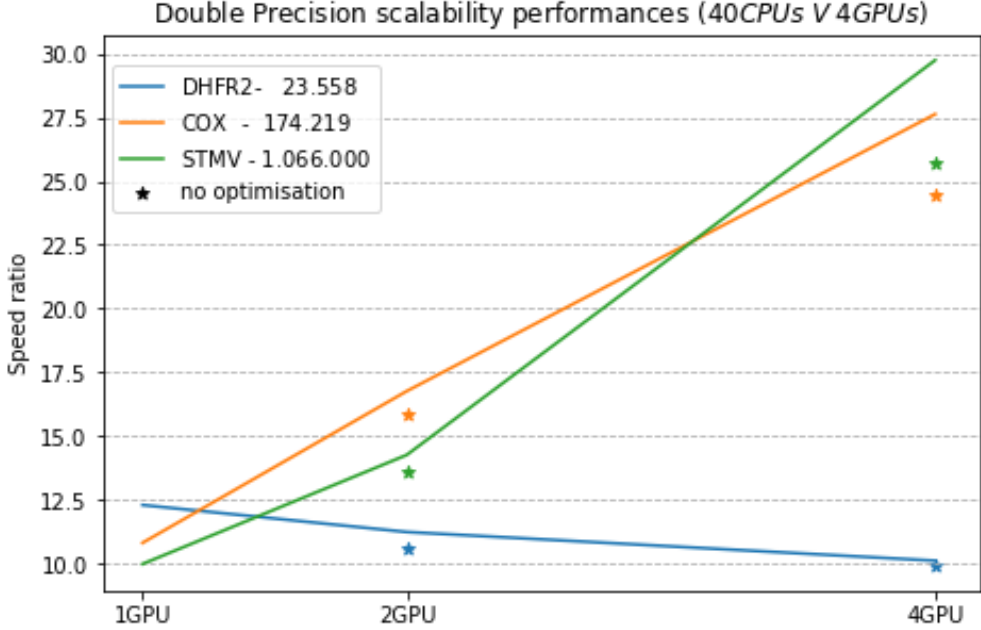


Figure 7: Performance ratio between single node GPU and single node CPU performance. Reference values can be found in [Table 1].

In summary, our DP implementation is already satisfactory compared to other applications such as Tinker-OpenMM. Our next section concerns the porting of Tinker-*HP* in single and mixed precision. As a reminder, our main goal is to provide an efficient *GPUs* implementation of PFF in Tinker-*HP* which can deliver high performances and good accuracy in every computational mode in addition of providing new scientific methods and features.

CUDA Approach

Even though we already have a robust OPENACC implementation of Tinker-*HP* in double precision, we have noted a moderate gain in speed when switching directly from double to single precision which is not consistent with device computational power (most *GPUs* have

much more compute power in SP compared to DP). This is more visible for devices with Geforce architecture because such cards do not possess DP physical compute units: a factor of 2 on Quadro GV100 and 31 on Geforce RTX 2080 Ti as their theoretical compute power goes respectively from 490 GFlops to 13.80 Tflops and 7 Tflops in double to 14 Tflops when switching precision. In general, GPUs are still more suited to SP arithmetic compared to CPUs.

More specifically, instead of doubling the simulation speed on V100 cards, we ended up noticing a 1.25 increase factor on V100 and 3 on RTX on DHFR2 in SP compared to DP with the same setup. All tests were done under the assumption that our simulations are valid in this precision mode. More results are to be found in [Table 2]. Furthermore, a deep profile conducted on the kernels constituting Tinker-*HP*’s bottleneck - real space non-bonded interactions - in the current state reveals an insufficient exploitation of the GPU SP compute power. [Figure 8] suggests that there is still room for improvements in order to take full advantage of the card’s computing power and memory bandwidth both in SP and DP . In order to exploit device SP computational power and get rid of the bottleneck exposed by [Figure 8], it becomes necessary to reshape our implementation method and consider some technical aspects beyond OPENACC ’s scope.

Table 2: Single precision MD production (ns/day) within the OPENACC implementation

	DHFR2	COX	STMV
V100	11.69	1.72	0.15
RTX-2080 Ti	11.72	1.51	n/a

Global overview and definitions

As mentioned in the previous section, *GPUs* are the most efficient with parallel computations and coalescent memory access patterns. This notion is very close to SIMD vectorization^{22,44} but with the possibility to apply it at a very large scale. This is the concept of Single Program Multiple Data (SPMD) approach. To improve the results presented in the last paragraph

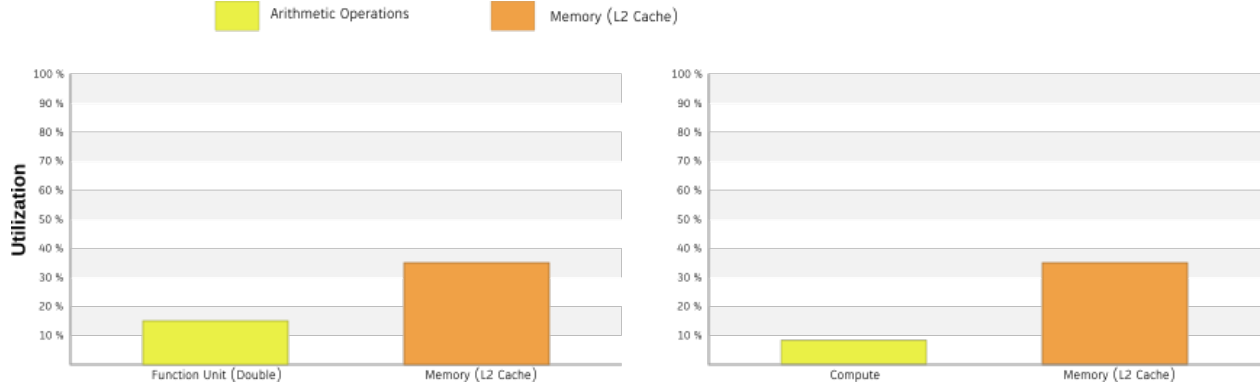


Figure 8: Profile of the matrix-vector compute kernel on the DHFR2 system. The left picture is obtained from the double precision run and the right one from simple precision. In both modes, results indicate an obvious latency issue coming from memory accessing pattern which prevents the device to reach its peak performance.

[Table 2] and to reach peak performance on computation and throughput, it becomes crucial to expose more computation in real space kernels and to minimize global memory accesses to benefit from cache & shared memory access on the other hand. To achieve that, we decided to rewrite those specific kernels using the standard approach of low-level device programming in addition to CUDA built-in intrinsics. We describe our corresponding strategy in a following section, but let us first review the issue of the precision.

Precision study and Validation

Definition i. We shall call ϵ_p the machine precision (in SP or DP), the smallest floating point value such that $1 + \epsilon_p > 1$.

Definition ii. Considering a positive floating point variable a , the machine precision ϵ_a attached to a is

$$1 + \epsilon > 1 \iff a + \epsilon_p * a > a \iff \epsilon_a = \epsilon_p * a$$

Therefore an error made for a floating point operation between a and b can be expressed as

$$a \tilde{\oplus} b = (a \oplus b) (1 + \epsilon_p)$$

where $\tilde{\oplus}$ designates the numerical operation between a and b .

Property i. Numerical error resulting from sequential reduction operations are linear while those resulting from parallel reduction are logarithmic. Thus, parallel reductions are entirely suitable to *GPUs* implementation as they benefit from both parallelism and accuracy.

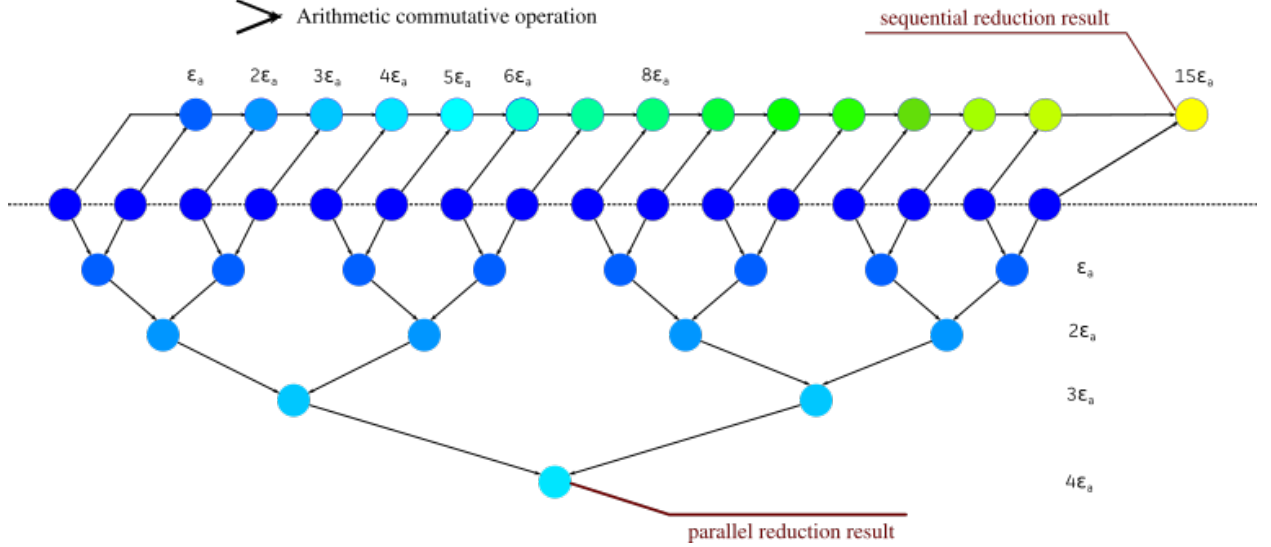


Figure 9: Reduction operation illustration on a 16 variables set. Each arithmetic operation generates an error ϵ_a that is accumulated during the sequential operation. On the other hand, parallel reduction uses intermediate variables to significantly reduce the error.

Before looking further into the matter of downgrading precision, we have to make sure that our application is able to work in this mode. Although it has been proven in the literature^{25,27,45} that many MD applications are able to provide correct results with simple precision, extensive precision studies with polarizable force fields are lacking. Even if applications like OpenMM operate on GPU devices at this mode, let us justify the use of this precision mode.

When it comes to floating point arithmetics, standard 32 storage bits offer no more than 7 significant digits due to the mantissa. In comparison, we benefit from 16 significant digits with DP 64 storage bits. Without any consideration on the floating number's sign, it is safe to assume that any application working with values outside $[10^{-7}, 10^7]$ scope will fail to deliver sufficient accuracy when running in complete DP mode. To overcome this matter, the common solution is to use a mixed precision mode which encompasses both modes by

using DP on variables subject to overflowing (in practice interactions are computed in SP but accumulated in DP). This way, we maintain a good accuracy on those entities.

All inputs in Tinker-*HP* - system data and parameters - are accessible to SP . Then, the same checks with the outputs (energy, force, pressure, ...) has to be made. The description made in the previous section shows that energy evaluation along with virial calculation are linear-dependent with the system's size. Depending on the complexity of the interaction in addition to the number of operations it requires, we can attach a constant error value named ϵ_i to it. Thus, we can bound the error made on the computation of a potential energy with $N_{int}\epsilon_i < n\text{Neig}_{max}\epsilon_i$ where N_{int} represents the number of interactions contributing to this energy. As this one is linear with respect to the system size we have to evaluate this entity with a DP storage container. Furthermore, to reduce even more the accumulation of error due to large summation, we shall employ buffered parallel reduction instead of sequential reduction [Figure 9]. On the other hand, we have to deal with the forces which remain the principal quantities which drive a MD simulation, in addition to other MD quantities: positions, speed, acceleration, timestep. Based on the fact that forces are also resulting from a pairwise interactions summation, the error made for each atom on the non bonded forces is bound by $\text{Neig}_{max} * \epsilon_i$ depending of course of d_{cut} .

However, each potential comes with a different ϵ_i . Our study estimates that the corresponding highest values ate the one of both van der Waals and bonded potentials. The high amount of pairwise interactions induced by van der Waals cutoff distance in addition to the computation method which includes power of 14 (for AMOEBA) on the distance comes close to a SP overflowing situation. We managed to overcome this potential issue with a traditional variable change technique applied on the pairwise computation. By reshaping the target variable, we get a result much closer to DP since intermediate calculations do not overflow. Regarding the bonded terms, ϵ_i depends more on the conformation of the system. Furthermore, we must take under consideration the fact that unlike the energy, a sequential reduction using atomic operations is applied to the forces. The resulting error is therefore

linear with the total number of summation operations. All those arguments led us to select a DP container on those entities despite the fact they can be held in an SP container. A practical verification of our theoretical analysis has been conducted once our hybrid/mixed precision (MP) implementation has been achieved. The results are represented in [Figure 10]. The fixed precision arithmetic is also a good choice for small to medium systems. Our interpretation of those results is that Tinker-*HP* is fine with mixed precision simulations. However, as one can see, if errors remain very low for forces even for large systems, a larger error exists for energies, a phenomenon observed in all previous MD *GPUs* implementations. Forces being the driving components of a molecular dynamic, the trajectories generated by our mixed precision implementation are accurate. To assess the error on the energies, 2 setups have been tested using single precision for pairwise computation: an energy accumulation approach with DP (default) and an other with a fixed precision (FP) setup inspired by the work of Walker, Götz et al.⁴⁵ and currently in development within Tinker9 (Z. Wang, in progress). The use of fixed precision do improve errors on energies about an order of magnitude but errors still increase linearly with the system size. However, it is true that for some specific post-treatment computations requiring energies, like in a BAR free energy computation, accurate values could be important especially for very large systems. In such a situation, one could use the double precision capabilities of the code for this post-processing step as Tinker-*HP* remains extremely efficient in DP even for large systems. In any case, the 3 possibilities will be ultimately proposed in Tinker-*HP*. A further validation simulation in the NVE ensemble can be found in [Figure 15] confirming the overall excellent stability of the code.

Neighbor list

We want to expose the maximum of computation inside a kernel using the device shared memory. To do so, we consider the approach where a specific group of atoms interacts with another one in a block-matrix pattern (see [Figure 11]). We need to load the parameters of

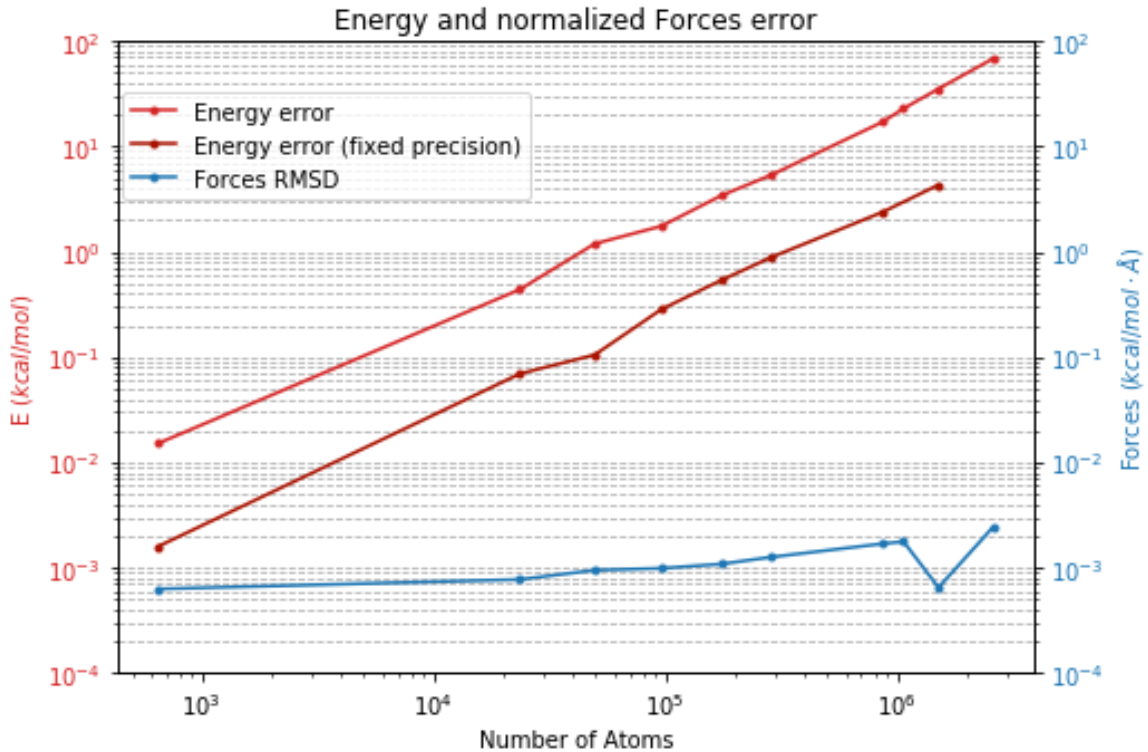


Figure 10: Absolute error between double precision implementation and mixed precision implementation on total potential energy. Forces root mean square deviation between DP and MP for systems from 648 up to 2 592 000 atoms. As expected, error on the energy grows linearly with the system size. Logarithmic regression gives 0.99 value for the curve slope. We reach 70 kcal/mol on the highest system. The relative energy for all systems is located under 1×10^{-5} . Regarding forces, the slight variations are due to the sensibility of the bonded forces to the conformation of the system: we can either obtain a slight growing error or an accurate RMSD like the 1 509 506 atoms test case. These numbers justify the use of Tinker-*HP* in mixed precision mode to perform accurate sampling.

the group of atoms and the output structures needed for computation directly inside cache memory and/or registers. On top of that, CUDA built-in intrinsics can be used to read data from neighbor threads and if possible compute cross term interactions. Ideally, we can expose $B_{comp} = B_{size}^2$ computations without a single access to global memory, with B_{size} representing the number of atoms within the group. With this approach, the kernel should reach its peak in terms of computational load.

A new approach of the neighbor list algorithm is necessary to follow the logic presented above. This method will be close to standard blocking techniques used in many MD applications.^{25,27} Let us present the structure of the algorithm in a sequential and parallel - MPI - context.

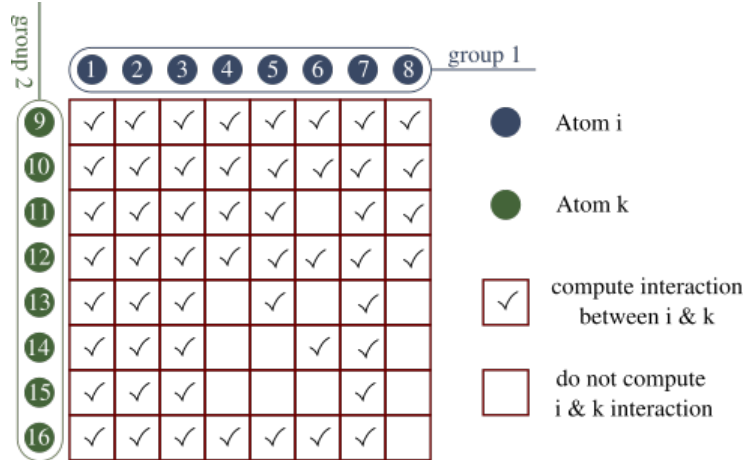


Figure 11: Representation of interactions between two groups of atoms within Tinker-HP. $B_{size} = 8$ for the illustration

Box partitioning

Lets us recall that given a simulation box Ω , a set of ω_c with $c \in [0..N_c]$ forms a Ω partition if and only if

$$\left\{ \begin{array}{l} \omega_1 \cup \dots \cup \omega_{N_c} = \Omega \\ \omega_1 \cap \dots \cap \omega_{N_c} = \emptyset \end{array} \right.$$

We consider in the following that each group deals with interactions involving atoms

within a region of space. In order to maximize B_{comp} between every pair of groups, we must then ensure their spatial compactness. Moreover, all these regions need to define a partition of Ω to make sure we do not end up with duplicate interactions. Following this reasoning, we might be tempted to group them into small spheres but it is impossible to partition a polygon with only spheres; not to mention the difficulties arising from the implementation point of view.

The MPI layer of Tinker-*HP* induces a first partition of Ω in P subdomains $\psi_p, p \in [0..P]$ where P is the number of MPI processes. Tinker-*HP* uses the midpoint image convention⁴⁶ so that the interactions computed by the process assigned to ψ_p are the ones whose midpoint falls into ψ_p . The approach used in Tinker-*HP* for the non bonded neighbor list uses a cubic partition $\omega_c, c \in [1..N_c]$ of ψ_p and then collects the neighboring atoms among the neighboring cells of ω_c . Here, we proceed exactly in the same way with two additional conditions to the partitioning. First, the number of atoms inside each cell ω_c must be less or equal than B_{size} . Second, we must preserve a common global numbering of the cells across all domains ψ_p to benefit from a unique partitioning of Ω .

Once the first partitioning in cells is done, an additional sorting operation is initiated to define groups so that each of them contains exactly B_{size} spatially aligned atoms following the cell numbering (note that because of the first constrain mention earlier, one cell can contain atoms belonging to a maximum of two groups). More precisely, the numbering of the cells follows a one dimensional representation of the three dimension of the simulation box.

Now, we want to find the best partitioning of ψ_p in groups that will ensure enough proximity between atoms inside a group, minimizing the number of neighboring groups and consequently maximizing B_{comp} .

When the partitioning generates too flat domains, each group might end up having too many neighboring groups. The optimal cell shape (close to a sphere) is the cube but we must not forget the first constrain and end up with a very thin partition either. However,

atom groups are not affected by a partition along the inner most contiguous dimension in the cell numbering. We can exploit this to get better partitioning. [Figure 12] illustrates and explains the scheme on a two dimensional box. Partitioning is done in an iterative manner by cycling on every dimension. We progressively increase the number of cells along each dimension starting on the contiguous one until the first condition is fulfilled. During a parallel run, we keep track of the cell with the smallest number of atoms with a reduction operation. This allows to have a global partitioning of Ω and not just ψ_p .

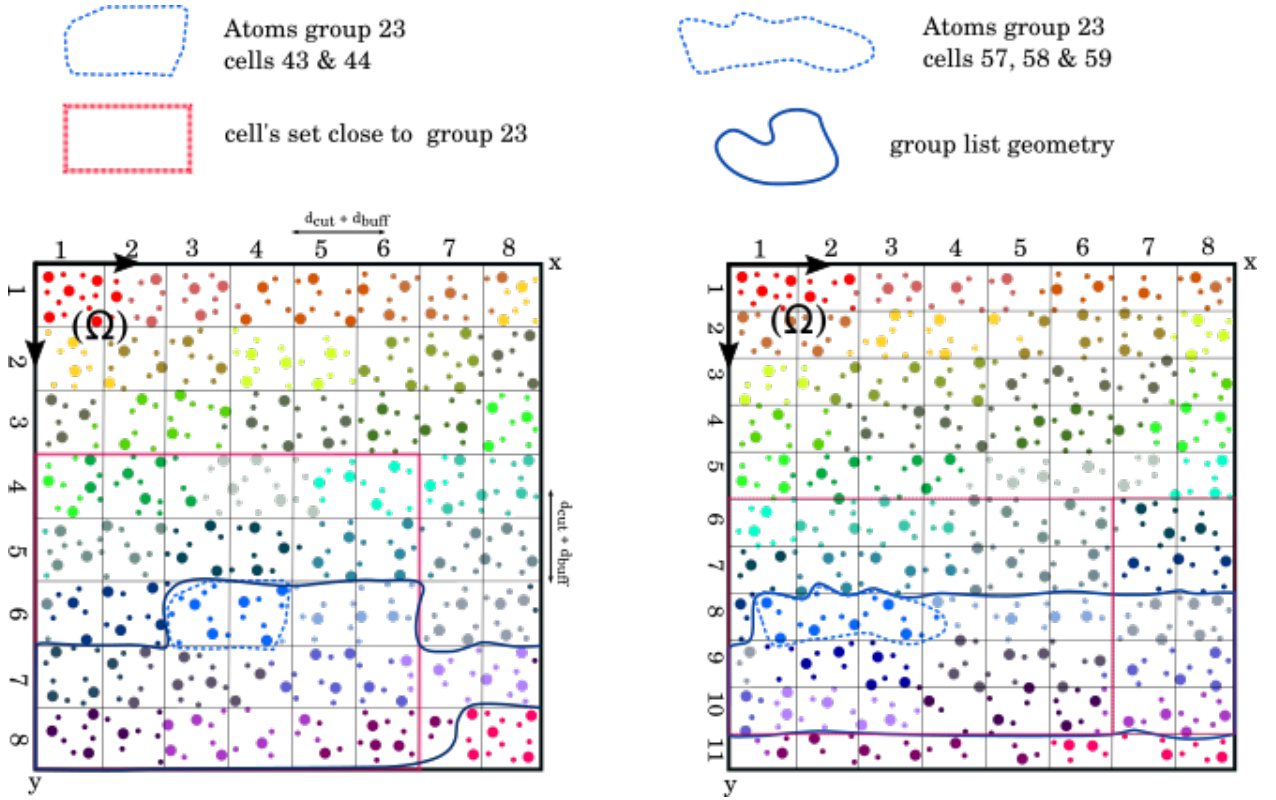


Figure 12: Illustration of a two dimensional Water Box partition along with groups. The left Figure shows a 64 cells partition of Ω while the right one refines this partitioning into 88 cells. Re-indexing all the atoms following the cells numbering and separating them equally shows all the groups. Here $B_{size} = 16$. A unique color is associated to every atom belonging to the same group. No cell contains more than B_{size} atoms or 2 groups. Once a group is selected -23-, searching for its neighboring groups is made through the set of cells (with respect to the periodic boundary condition) close to the cells it contains - 43 & 44 -. Once this set is acquired, all the group indexes greater or equal than the selected group constitute the actual list of neighbors to take the symmetry of the interactions into account. We see that the group's shape modulates the group neighborhood as illustrated with the right illustration and a spatially flat group 23.

Now that we do dispose of a spatial rearrangement of the atoms into groups, we need to construct pair-lists of all interacting groups according to the cutoff distance plus an additional buffer to avoid reconstructing it at each time step. It is relatively straightforward given the way each group is defined. They are built in such a way that it is straightforward to jump from groups indexing to cells indexing. The approach we have chosen goes through a construction of an adjacency matrix first. The reason behind this choice stands in its convenient attribute of being *GPUs* suitable and compatible with the MPI parallelism. Once built, the adjacency matrix directly gives the pair-list. Regarding the storage size involved with this approach, note that we only require single bit to tag pair-group interactions. This results in an $\lceil \frac{n_l}{B_{size}} \rceil^2$ bits occupation which equals to $\lceil \frac{n}{B_{size}} \rceil^2 \frac{1}{8}$ bytes. n_l represents the number of atoms which participates to real space evaluation on a process domain (ψ_p). Of course, in terms of memory we cannot afford a quadratic reservation. However the scaling factor $\lceil \frac{1}{B_{size}} \rceil^2 \frac{1}{8}$ happens to be small enough even for the smallest value of B_{size} set to 32 in accordance to device warp size. Not to mention that, in the context of multi-device simulation, the memory distribution is also quadratic. The pseudo-kernel is presented in [Listing 3]

```
c$acc parallel loop default(present)
do i = 1, numCells
    celli = i
    !get blocks_i inside celli
    ...
c$acc loop vector
do j = 1, numCellsNeigh
    ! Get cellj with number
    ...
    ! Get blocks_j inside cellk
    ...
    ! Apply symmetrical condition
    if ( cellj > celli ) cycle
c$acc loop seq
    do bi in blocks_i
        do bj in blocks_j
c$acc atomic
        set matrix(bj,bi) to 1
```

```

    end do
  end do
end do
end do

```

Listing 3: Adjacency matrix construction pseudo-kernel. We browse through all the cells and for each one we loop on their neighbors. It is easy to compute their ids since we know their length as well as their arrangement. Since all the cells form a partition of the box we can apply the symmetrical condition on pair-cells; we retrieve the groups inside thanks to the partitioning condition which ensures that each cell contains at most two groups. Pair-blocks matrix location are therefore marked.

Once the adjacency matrix is built, a simple post-processing gives us the adjacency list with optimal memory size and we can use the new list on real space computation kernels following the process described in the introduction of this subsection and illustrated in [Figure 11]. In addition, we benefit from a coalesced memory access pattern while loading blocks data and parameters when they are spatially reordered.

List filtering

We can improve the performance of our group-group pairing with an approach similar to the list reordering method mentioned in the optimizations presented above. The principle is to filter every neighboring group in order to get a list of atoms which really belong to a group's neighborhood. The process is achieved by following the rule:

$$\alpha \in \mathcal{B}_I \quad \text{if } \exists \alpha_i \in \beta_I \quad \text{such that } \text{dist}(\alpha_i, \alpha) \leq d_{\text{cut}} + d_{\text{buff}}.$$

α and α_i are atoms, β represents a group of B_{size} atoms, \mathcal{B} is the neighborhood of a group and $\text{dist} : (\mathbb{R}^3 \times \mathbb{R}^3) \rightarrow \mathbb{R}$ is the euclidean distance.

An illustration of the results using the filtering process is depicted in [Figure 13].

After extracting this new list of atoms, it is reinterpreted as a set of groups on which to

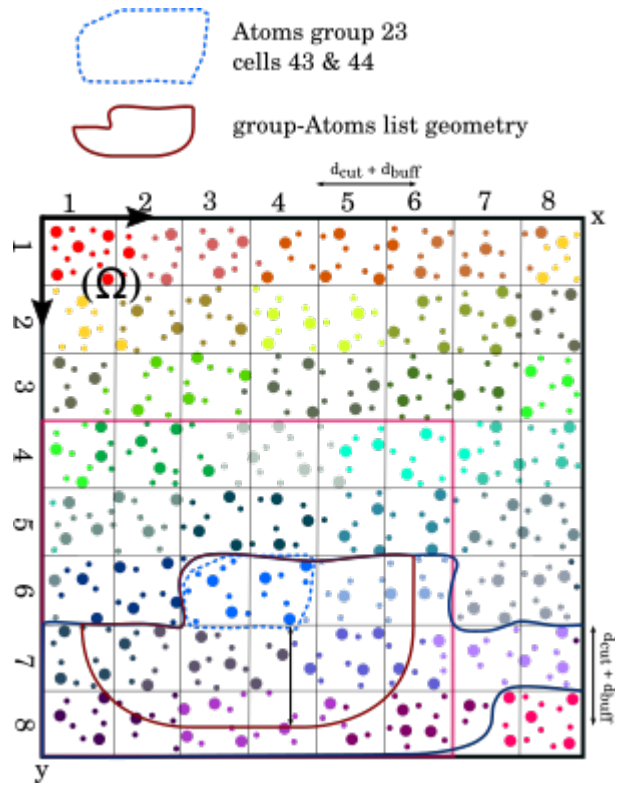


Figure 13: Starting from the latest Figure 12, we represent the geometry resulting from the filtering process. As observed in comparison with the previous list, we significantly reduce group 23 neighborhood with the list filtering- From 144 atoms with the first list to 77 with the filtered one -. B_{comp} increases which corresponds to more interactions computed within each group pair.

interact. When the number of neighbor atoms is not a multiple of B_{size} , we create phantom atoms to complete the actual neighbor lists. A drawback of the filtering process is a loss of coalesced memory access pattern. As it has been entirely constructed in parallel, we don't have control of the output order. Nonetheless, this loss is compensated by an increase of B_{comp} for each interaction between groups, as represented by [Figure 13]. In practice, we measure a 75% performance gain between the original list and the filtered one for the van der Waals interaction kernel. Moreover, [Figure 14] (deep profile of the previous bottleneck kernel: matrix-vector product) shows a much better utilisation of the device computational capability. We applied the same strategy for the other real space kernels (electrostatics and polarization).

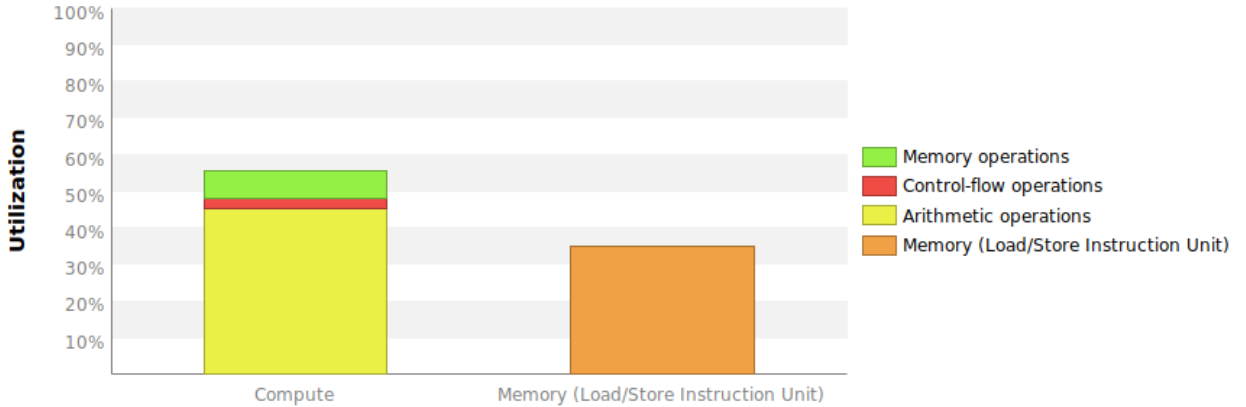


Figure 14: Real space kernel profiling results in mixed precision using our new group-Atoms list.

PME separation

As mentioned above, the Particle Mesh Ewald method separates electrostatics computation in two spaces - real and reciprocal -. A new profiling of Tinker-*HP* in single-device mixed precision mode with the latest developments shows that the reciprocal part is the new bottleneck. More precisely, real space performs 20% faster than reciprocal space within a standard PME setup. Moreover, reciprocal space is even more a bottleneck in parallel because of the additional MPI communications induced by the **cuFFt** Transformations. This significantly

narrow our chances of benefiting from the optimizations mentioned in the previous optimization subsection. However, as both parts are independent, we can distribute them on different MPI processes in order to reduce or even suppress communications inside FFT's. During this operation, a subset of *GPUs* are assigned to reciprocal space computation only. Depending on the system size and the load balancing between real and reciprocal spaces, we can break through the scalability limit and gain additional performance on a multi-device configuration.

Mixed precision validation

The precision study already showed that Tinker-*HP* will be suited to mixed precision simulations. At least when it comes to molecular dynamics using PFF, the error made during forces evaluation is almost constant with the system size. In other words, we are safe from floating point overflow in addition to benefiting from a correct accuracy consistent with double precision simulations. To validate our implementation, we compare a 1 nanosecond long simulation in double precision on CPU (Tinker-*HP* 1.2) in a constant energy setup (NVE) with the exact same run using the GPU mixed precision implementation, using a 0.5 fs time step and the DHFR2 solvated protein [Figure 15]. We see that using the mixed precision GPU implementation, the total energy fluctuates within -1 and 3 kcal/mol during the run, showing the good accuracy of the simulation in this mode.

Available Features

After this validation, we focused on porting the main features of Tinker-*HP* to the GPU implementation such as its various integrators like the new multi-time step integrators: RESPA1 and BAOAB-RESPA1⁴⁷ which allows to use up to a 10 fs time step with PFF (this required to create new neighbor lists to perform short-range non-bonded interactions computations for both van der Waals and electrostatics). Aside from Langevin integrators, we ported the Bussi⁴³ (which is the default) and the Berendsen thermostats, as well as the Monte-Carlo

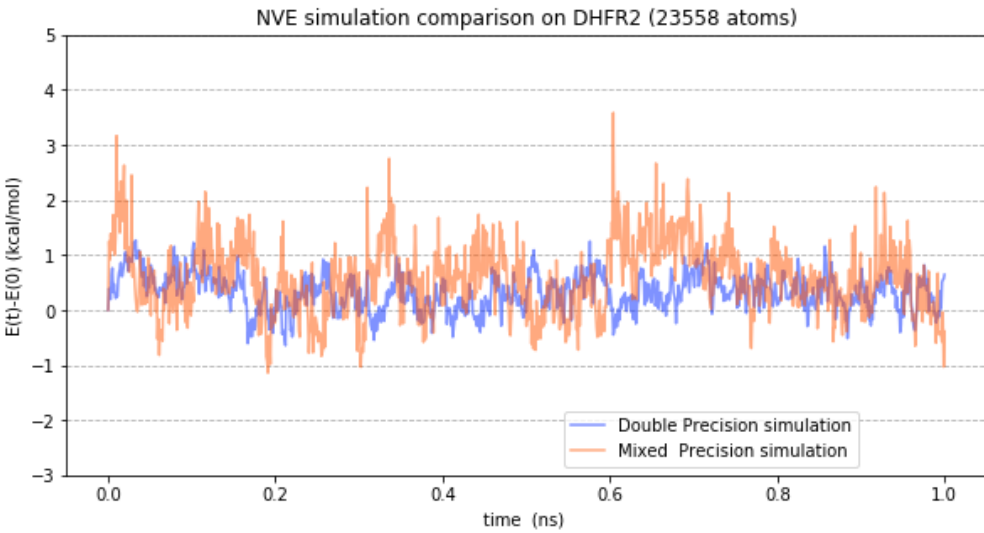


Figure 15: Variation of the total energy during a NVE molecular dynamics simulation of the DHFR2 protein in both DP and mixed precision.

and the Berendsen barostats. We also ported free energy methods such as the Steered Molecular Dynamics⁴⁸ and van der Waals soft cores for alchemical transformations, as well as the enhanced sampling method Gaussian Accelerated Molecular Dynamics.⁴⁹ Even if it is not the main goal of our implementation as well optimized softwares suited to such simulations exist, we also ported the routines necessary to use standard non-polarizable force fields such as CHARMM,⁴ Amber⁵ or OPLS.⁵⁰ Still, we obtained already satisfactory performances with these models despite a simple portage, the associated numbers can be found in supplementary information and further optimization is ongoing. On top of all these features that concern a molecular dynamics simulation, we ported the "analyze" and "minimize" program of Tinker-HP, allowing to run single point calculations as well as geometry optimizations. All these capabilities are summed up in table 3

Performance and Scalability Results

We ran benchmarks on various systems using our mixed precision implementation on *GPUs* on V100 nodes of the Jean-Zay supercomputer. We also ran the whole set of test on the Irène

Table 3: Available features in the initial Tinker-*HP* GPU release

Programs	dynamic; analyze; minimize
Integrator	VERLET(default); RESPA; RESPA1; BAOAB-RESPA; BAOAB-RESPA1
Force fields	AMOEBA; CHARMM/AMBER/OPLS
Miscellaneous	Steered MD (SMD); Gaussian Accelerated MD; Restraints Groups; Soft Cores
Thermostat	Bussi(default); Berendsen
Barostat	Berendsen(default); Montecarlo

Joliot Curie ATOS Sequana supercomputer V100 partition to ensure for the portability of the code. We used two different integrators: (2 fs RESPA along with 10 fs BAOAB-RESPA1 with heavy hydrogens). For each system, we performed 2.5 ps and 25 ps MD simulations with RESPA and BAOAB-RESPA1 respectively. Van der Waals and real space electrostatics cutoffs were respectively set to 9 and 7 Å plus 0.7 Å neighbor list buffer for RESPA 1 Å for BAOAB-RESPA1. The Bussi thermostat has been used for the 300 K NVT RESPA simulation. Our test cases included, water boxes within the range of 96 000 atoms (i.e. **Puddle**) up to 2 592 000 atoms (i.e **Bay**), the **DHFR2**, **COX** and the Main Protease of Sars-Cov2 proteins (**M^{pro}**)⁵¹ as well as the **STMV** virus.

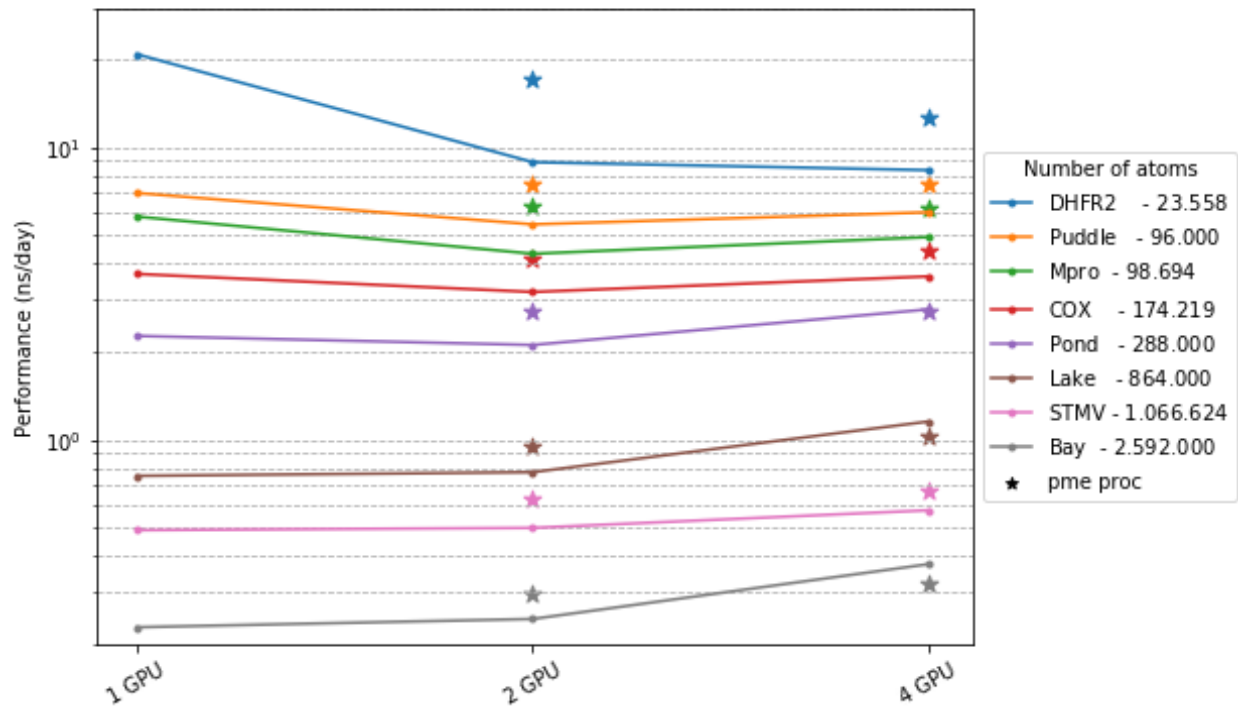
[Figure 16] recaps all the performance results and the number of atoms of the systems. On a single GPU device, the BAOAB-RESPA1 integrator performs almost twice as fast as RESPA in all test cases - 20.81 to 37.91 ns/day on **DHFR2**, 0.49 to 1.06 ns/day for the **STMV** virus. Regarding the RESPA integrator, results compared with those obtained in DP are now close to the Quadro V100 theoretical performance [Table 1]. Speeds ratio are now respectively of 2.24-fold for **DHFR2** and 3.88 for **STMV**. This reinforces our assumption according to which the first implementation - with standard neighbor list - is not suited to bigger systems like **STMV**. On the other hand, the parallel scalability starts to be effective above 100 000 atoms. With RESPA, we observe a speed ratio between 1.06 to 1.68 respectively on **M^{pro}** and **bay** benches on 4 *GPUs* compared to a single one. The relatively balanced load between real and reciprocal space with RESPA allows us to break through the scalability limit on almost every *GPUs* simulations with 2 *GPUs* with PME separation enabled. For instance, for the **STMV** case, we have a better performance on 2*GPUs* with PME separation

than with *4GPUs* without (0.62 ns/day V 0.57 ns/day), knowing that *2GPUs* only benefits from a quarter of interconnection bandwidth available on a node. Such a delay in the strong scalability is understandable given the device computational speed and the messages size imposed by the system and the configuration run. For example, we noticed that for the *stmv* system using *4GPUs* and *BAOAB-RESPA1*, communications represents 65% of a timestep. This is an indication of the theoretical gain we can obtain with an improvement of the interconnect technology or the MPI layer. Nevertheless, it is already satisfactory to be able to scale on huge systems since one of the goals of the development of *Tinker-HP* is to efficiently tackle systems containing up to several millions of atoms.

Table 4 shows the performance obtained on a single Geforce RTX-2080 Ti with both *RESPA* and *BAOAB-RESPA1* frameworks. We observe similar absolute performances compared to the Jean-Zay V100s for systems up to 100 000 atoms, and the same doubling in performance by using *BAOAB-RESPA1*. For larger systems, V100 results exceeds the RTX ones.

Furthermore, we compared the performance of our code to an already existing implementation of PFF on *GPUs* on a V100: *Tinker-OpenMM* with a similar *RESPA* framework and observe between 12 and 30% of performance increase depending on the systems.

Tinker-HP GPU scalability (Jean Zay Cluster)
RESPA 2fs



Tinker-HP GPU scalability (Jean Zay Cluster)
BAOAB-RESPA1 10fs

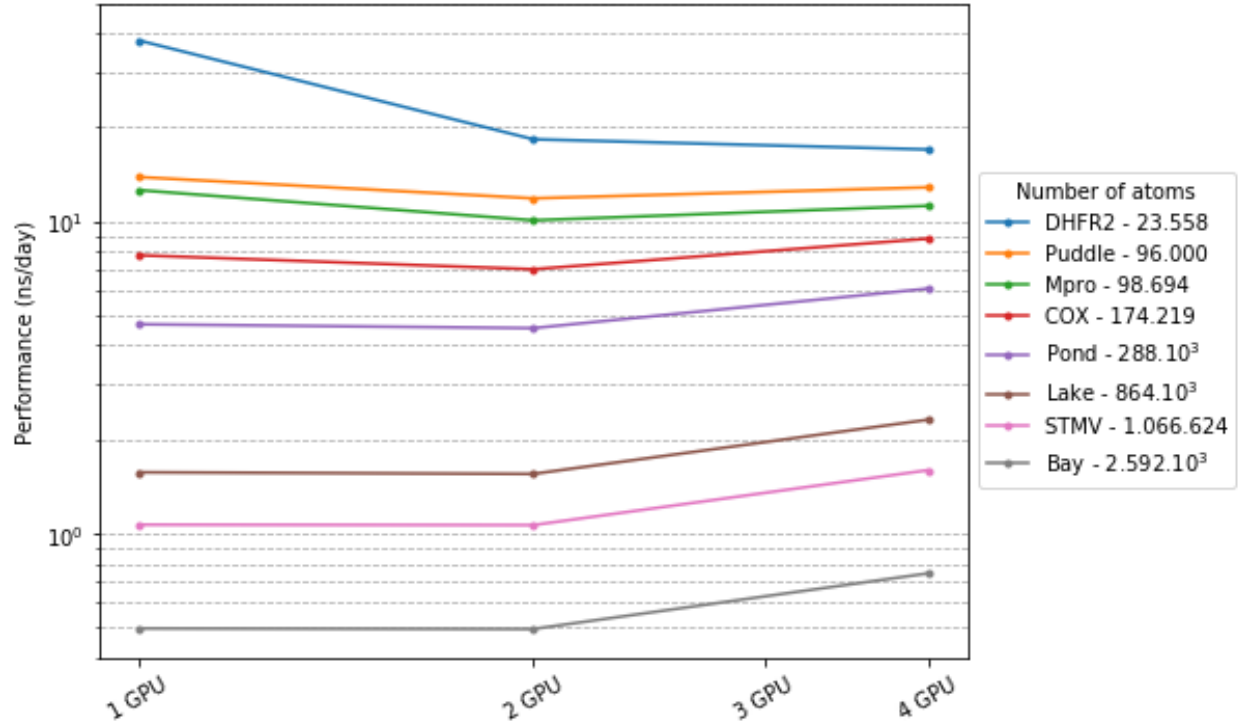


Figure 16: Single node mixed precision scalability on the Jean Zay Cluster (V100) using the AMOEBA polarizable force field

Table 4: Mixed precision performances assessed on single Geforce RTX-2080 Ti GPU card

Systems	DHFR2	M^{pro}	COX	Pond	Lake	STMV	Bay
RESPA 2fs (ns/day)	20.99	4.98	2.97	1.70	0.51	0.31	0.14
BAOAB- RESPA1 10fs (ns/day)	39.98	11.06	6.56	3.87	1.20	0.76	n/a

Table 5: Mixed precision performances assessed on single Quadro GV100 with RESPA Integrator at 2fs

Systems	DHFR2	M^{pro}	COX	Pond	Lake	STMV	Bay
Tinker- <i>HP</i> (ns/day)	19.75	5.58	3.40	2.09	0.68	0.44	0.20
Tinker-OpenMM (ns/day)	17.53	4.50	2.56	1.68	0.56	0.34	n/a

Towards larger systems

We reviewed in the last section the impressive performance obtained by the porting of the Tinker-*HP* application to *GPUs* in mixed precision. However one of the goals of the development of Tinker-*HP* is to be able to treat (very) large biological systems such as protein complexes or entire viruses encompassing up to several millions of atoms. Clearly since march 2020, the present development efforts were reoriented towards enabling the extensive modeling of SARS-Cov-2 proteins using the AMOEBA polarizable force field. The *CPU* implementation already allowed the simulations of systems like the STMV virus by using several thousands of *CPU*s cores.^{20,22} The following section reviews the scalability limit of the GPU implementation in terms of system size knowing that *GPUs* don't have the same memory capabilities.

How far can we go in terms of system size on a single *GPUs* and at what point a multi-*GPUs* (potentially on several nodes) simulation becomes really useful? A critical aspect concerns memory: where classical *CPU* nodes routinely benefit from more than 128 GB of memory, the most advanced Ampere *GPU* architecture holds up to 40 GB of memory. Thus, it becomes crucial to study and optimize memory distribution in our *GPU* implementation.

Tinker-*HP* Memory management model

MD with 3D spatial decomposition has its own distribution pattern when it comes to memory distribution among MPI processes. We use the midpoint rule to compute real space interactions as it is done in the CPU implementation. In practice, it means that each process holds information about its neighbors (to be able to compute the proper forces). More precisely, a domain ψ_q belongs to the neighborhood of ψ_p if the minimum distance between them is under some cutoff distance plus a buffer. To simplify data exchange between processes, we transfer all positions in a single message, the same thing is done with the forces. An additional filtering is then done to list the atoms actually involved in the interactions computed by a domain ψ_p . An atom $\alpha \in \Omega$ belongs to domain ψ_p 's interaction area (λ_p) if the distance between this atom and the domain is below $\frac{d_{cut}+d_{buff}}{2}$.

Lets us call n_p the number of atoms belonging to the ψ_p domain, n_b the number of atoms belonging to a process domain and its neighbors and n_l the number of atoms inside λ_p . This is illustrated in [Figure 17].

One can see that all data reserved with a size proportional to n_p are equally distributed among processes. Those with size proportional to n_b are only partially distributed. In other words, the distribution for these data strucures is non-existent if all domains ψ_p are neighbors. This is why in practice the distribution only takes place at that level with a relatively high number of process - more than 26 at least on a large box with 3d domain decomposition -. On the other hand, data allocated with a size proportional to n_l like the neighbor list see their distribution increase with the number of processes depending on the

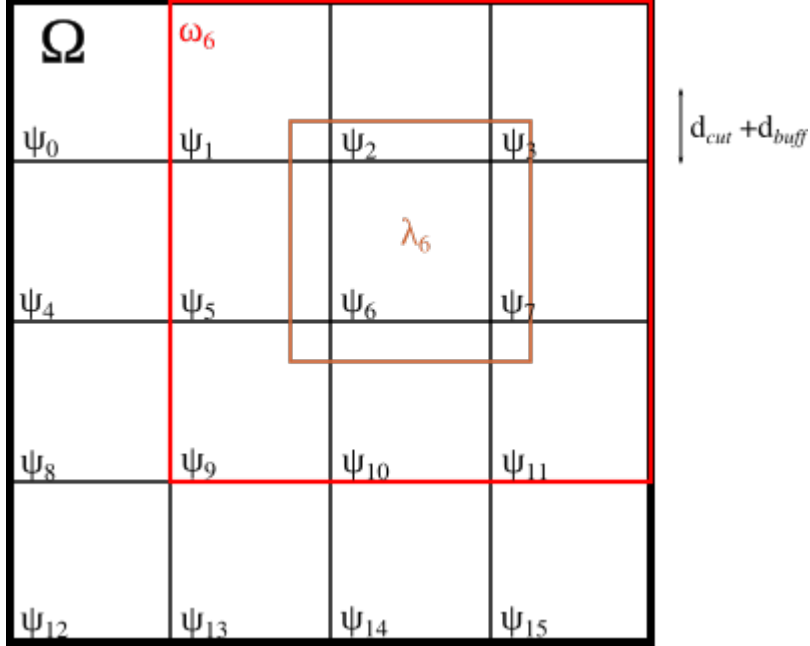


Figure 17: Two dimensional spatial decomposition of a simulation box with MPI distribution across 16 processes. ω_6 collects all the neighboring domains of ψ_6 . Here $\mathbf{n}_b < \mathbf{n}$

fact that \mathbf{n}_l is more close to \mathbf{n}_p than \mathbf{n}_b . On top of that, some data remains undistributed (proportional to \mathbf{n}) like atom parameters for each potential energy term. Splitting those among MPI processes would severely increase the communication cost which we can not afford. As we cannot predict how one atom will interact and move inside the box Ω , the best strategy regarding such data is to make all parameters available to each process. Reference Tinker-*HP* reduces the memory footprint of such data by using MPI shared memory space. Thus, only one parameter data instance is shared among all processes within the same node.

When it comes to multi-*GPUs* simulations, there is no such things as shared memory between *GPUs* inside a node. The only way to deal with undistributed data is by replicating all of them on each device. This approach will have serious consequences on memory with large systems: as the system size increases, so does the duplicated memory space. This limits the capability to reach huge systems on *GPU* platforms. Therefore, we are left with two solutions: waiting for next generations *GPUs* and their additional memory capabilities, or find a new approach to communicate information between devices. The latter is the topic of

the next section.

NVSHMEM feature implementation

As explained above, a parameter data distribution would necessarily result in additional communications. Regarding data exchange optimizations between *GPU* devices, NVIDIA develops a new library based on the OpenSHMEM⁵² programming pattern which is called NVSHMEM.²⁹ This library provides thread communication routines which operate on a symmetric memory on each device. That is to say, we have the possibility to initiate device communication inside kernels and not outside with an API like MPI. The immediate benefit of such approach resides in the fact that communications are automatically recovered by kernels instructions and can thereby participate to recover device internal latency. With this library, we have an unprecedented opportunity to distribute n scale data over devices within one node.

Our implementation follows this scheme. Divide a data structure (an array for instance) across devices belonging to the same node following the global numbering of the atoms and access this data inside a kernel with the help of NVSHMEM library. To achieve such implementation, we rely on a NVSHMEM feature which consists in storing a symmetric memory allocation address in a pointer on which arithmetic operations can be done. Then, depending on the address returned by the pointer, either a global memory access (GBA) or a remote memory access (RMA) is made to fetch the data. The implementation requires a Fortran interface to be operational since NVSHMEM source code is written in the C language. Moreover, an additional operation is required for every allocation performed by the NVSHMEM specific allocator in view of making the data allocated accessible through OPENACC kernels.

Such a singular approach affects performances since additional communications have to be made inside kernels. Furthermore, all communications do not follow a special pattern that would leave room for optimizations, meaning that each device accesses data randomly

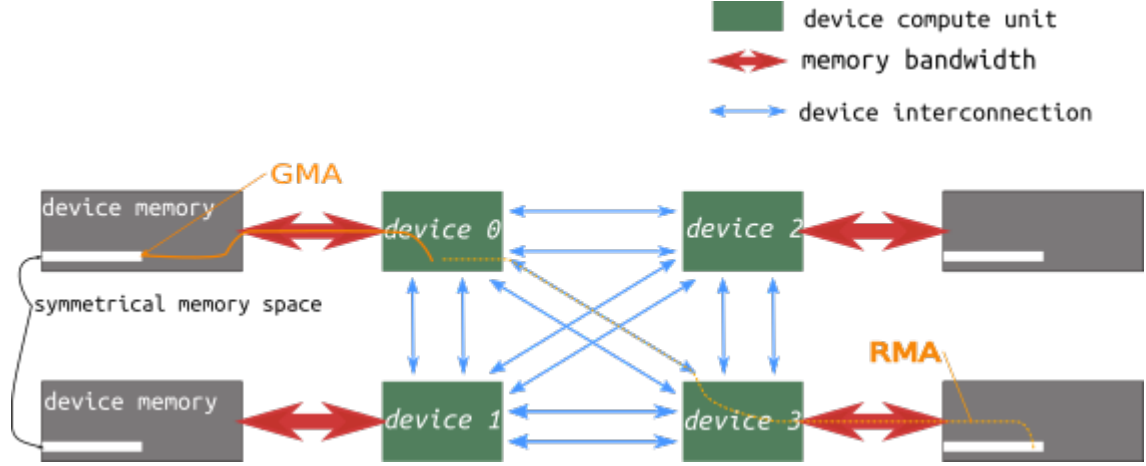


Figure 18: NVSHMEM memory distribution pattern across a four interconnected devices node. A symmetric reserved space is allocated by the NVSHMEM library at initialization. Thus, data is equally split across all devices in order. Every time a device needs to access data allocated with NVSHMEM, either a GMA or RMA is issued.

from the others depending on the atoms involved in the interactions it needs to compute. In order to limit performance loss, we can decide which data is going to be split across devices and which kernels are going to be involved with this approach. Considering the force fields of interest, it seems reasonable that affecting bonded force kernels with NVSHMEM feature is a good choice. Doing so, we aim to distribute most of the parameter data - which mainly concern bonded terms (torsions, angles, bonds,...) - and therefore reduce the duplicated memory footprint. We won't touch any undistributed data related to non-bonded interactions to keep those kernels unharmed.

Perspectives and additional results

During our NVSHMEM implementation, we were able to detect and optimize several memory wells. For instance, the adjacency matrix described in section 1. has a quadratic memory requirement following the groups of atoms. This means that this represents a potential risk of memory saturation on a single device. To prevent this, we have implemented a buffer limit on this matrix with the intention to construct the pair-group list piece by piece. We have also implemented algorithms that prioritize computing and searching over storing where ever

needed - essentially scaling factor reconstruction -. In the end, Tinker-*HP* is able to simulate a 7 776 000 atoms water box with a performance of 0.15 ns/day with the AMOEBA force field on a single V100 and scale-out to 0.25 ns/day on Jean Zay's one node.

Later in our progression, we had the opportunity to test our implementation on the latest generation NVIDIA *GPU* Ampere architecture: the Selene supercomputer whis is made of nodes consisting in DGX-A100 servers. A DGX-A100 server contains eight A100 graphic cards with 40 GB of memory each and with latest generation inter-connection NVIDIA Switches. The results we obtained on such a node with the same systems as above in the same RESPA and BAOAB-RESPA1 framework are listed in [Table 6] and [Figure 19].

We observe an average of 50% of performance gain for systems larger than 100 000 atoms on a single A100 compared to a single V100 card. Also, the more efficient interconnection between cards : NV-switch compared to NV-link, allows to scale better on several GPUs with the best performances ever obtained with our code on all the benchmark systems, the larger ones making use of all the 8 cards of the node. Although the code is designed to do so, the latency and the speed of the inter-node interconnection on the present Jean-Zay and Selene supercomputers did not allow us to scale efficiently accross nodes, even on the largest systems. The very fast evolution of the compilers, as well as the incoming availability of new classes of large pre-exascale supercomputers will change this situation. Presently, the use of multiple nodes for a single trajectory is the subject of active work within our group and results will be shared in due course. Still, one can already make use of several nodes with the present implementation by using methods such as unsupervised adaptive sampling as we recently proposed.⁵¹ Such pleasingly parallel approach already offers the possibility to use hundreds (if not thousands!) of GPUs card simultaneously.

Table 6: Performance synthesis and scalability results on the Jean Zay (V100) and Selene (A100) machines. MD production in ns/day with the AMOEBA polarizable force field

Systems	Size (NumAtoms)	Jean Zay (V100)		Selene (A100)	
		Perf (ns/day)	Peak Perf (ns/day)	Perf (ns/day)	Peak Perf (ns/day)
		- 1GPU	- #GPU	- 1GPU	- #GPU
DHFR2	23 558	37.91	37.91	39.35	39.35
Puddle	96 000	13.84	14.04 -4	15.57	17.57
M ^{pro}	98 694	12.57	12.97 -4	16.36	17.47 -4
COX	174 219	7.86	9.10 -4	10.47	11.75 -4
Pond	288 000	4.68	6.08 -4	6.18	10.60 -8
Lake	864 000	1.57	2.31 -4	2.11	5.50 -8
STMV	1 066 624	1.06	1.60 -4	1.50	4.51 -8
SARS-CoV2	1 509 506	0.89	1.39 -4	1.32	4.16 -8
Spike-ACE2					
Bay	2 592 000	0.50	0.74 -4	0.59	2.38 -8
Sea	7 776 000			0.22	0.78 -8

Conclusion

We presented the native Tinker-*HP* multi-*GPUs* - multi-precision acceleration platform. The new code is shown to be accurate and scalable across multiple *GPUs* cards offering unprecedented performances and new capabilities to deal with long timescale simulations on large realistic systems using polarizable force fields such as AMOEBA. The approach strongly reduces the time to solution offering to achieve routine simulations that would have required thousands of CPUs cores on a single *GPU* card. Overall, the *GPU* -accelerated Tinker-*HP* reaches the best performances ever obtained for AMOEBA simulations and extends the applicability of polarizable force fields. The package is shown to be applicable to various computer *GPU* system architectures ranging from research laboratories to modern supercomputers.

Future work that will lead to Tinker-*HP* 1.3 will focus on adding additional features (sampling methods, integrators ...) and on further optimizing the performance of the multi-nodes /multi-*GPUs* to address the exascale challenge. We will improve the non-polarizable force

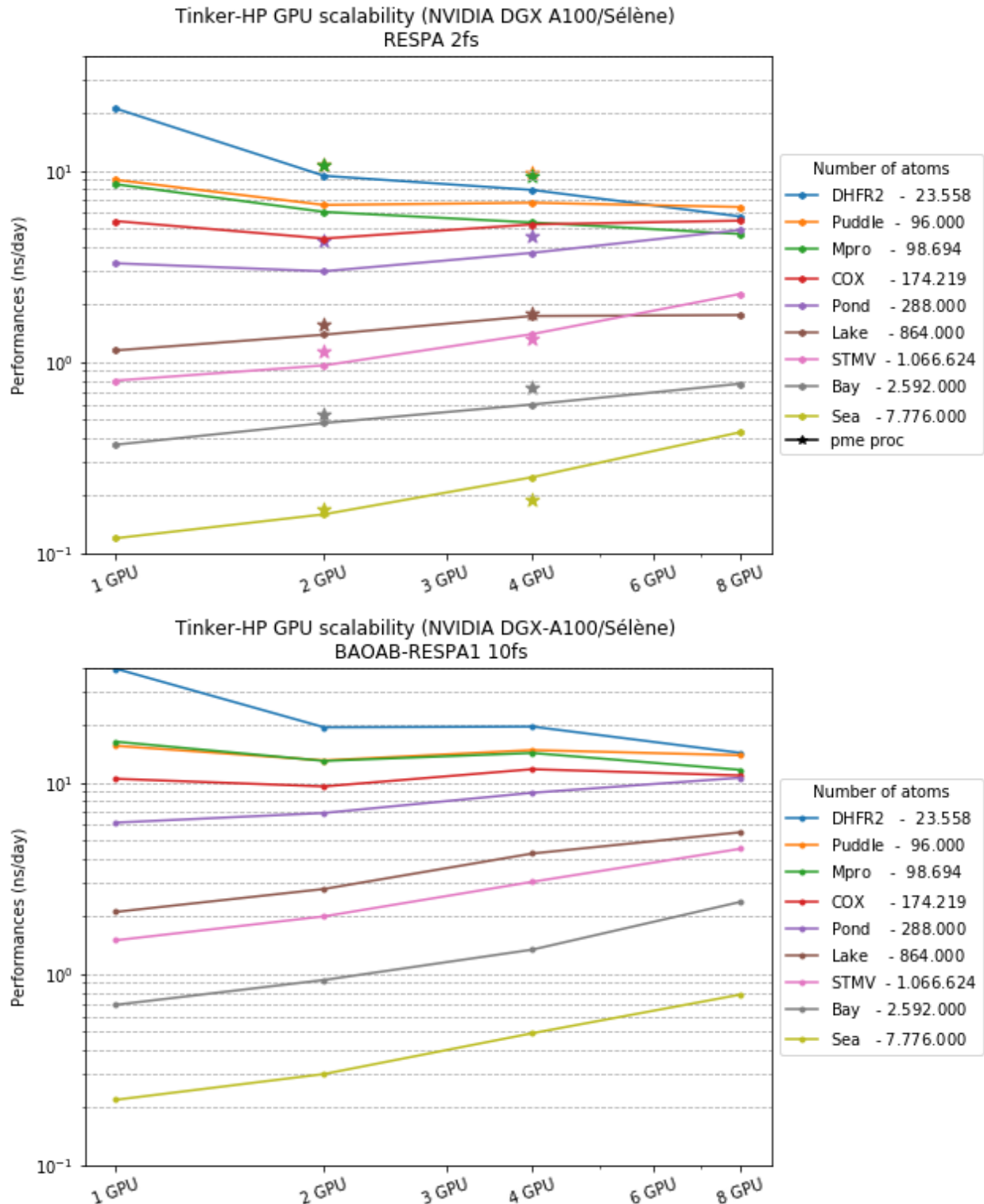


Figure 19: Performance and one node scalability results with the AMOEBA force field

field simulations capabilities as we will provide the high performance implementations of additional new generation polarizable many-body force fields models such as AMOEBA+,^{53,54} SIBFA⁵⁵ and others. Beyond this native GPU platform, Tinker-*HP*'s users will still conserve the possibility to use the latest OpenMM library thanks to an incoming interface in the spirit of the initial Tinker-OpenMM framework. We will continue to develop the recently introduced adaptive sampling computing strategy enabling the simultaneous use of hundreds (thousands) of *GPU* cards to further reduce time to solution and deeper explore conformational spaces at high resolution.⁵¹ Indeed, in such simulations that are grounded on the present *GPU* code have been the basis of our COVID-19 research, one can decompose the global proteins conformational space exploration problem into a set of separate MD trajectories that can be restarted within an iterative selection process able to achieve sufficient phase-space sampling within large biosystems. With such exascale-ready simulation setup, computations that would have taken years can now be achieved in days thanks to *GPUs*. Finally, this work, that extensively exploits low precision arithmetic, highlights the key fact that high-performance computing (HPC) grounded applications such as Tinker-*HP* can now efficiently use converged GPU-accelerated supercomputers, combining HPC and artificial intelligence (AI) such as the Jean Zay machine to actually enhance their performances.

Acknowledgements

This work was made possible thanks to funding from the European Research Council (ERC) under the European Union's Horizon 2020 research and innovation programme (grant agreement No 810367), project EMC2. This project was initiated in 2019 with a "Contrat de Progrès" grant from GENCI (France) in collaboration with HPE and NVIDIA to port Tinker-HP on the Jean Zay HPE SGI 8600 GPUs system (IDRIS supercomputer center, GENCI-CNRS, Orsay, France) using OpenACC. FC acknowledges funding from the French state funds managed by the CalSimLab LABEX and the ANR within the Investissements d'Avenir program

(reference ANR11-IDEX-0004-02) and support from the Direction Générale de l’Armement (DGA) Maîtrise NRBC of the French Ministry of Defense. Computations have been performed at GENCI on the Jean Zay machine (IDRIS) on grant no A0070707671 and on the Irène Joliot Curie ATOS Sequana X1000 supercomputer (TGCC, Bruyères le Chatel, CEA, France) thanks to PRACE COVID-19 special allocation (projet COVID-HP). We thank NVIDIA (Romuald Josien and François Courteille, NVIDIA France) for offering us access to A100 supercomputer systems (DGX-A100 and Selene DGX-A100 SuperPod machines). PR and JWP are grateful for support by National Institutes of Health (R01GM106137 and R01GM114237).

Code availability

The present code has been released in phase advance in link with the High Performance Computing community COVID-19 research efforts. The software is freely accessible to Academics via GitHub : <https://github.com/TinkerTools/tinker-hp>

Competing interest

The authors declare no competing interests.

Additional information

This information is available free of charge via the Internet at <http://pubs.acs.org>

List of Figures

1	OPENACC synchronous execution model on test kernel <fill>	6
2	OPENACC asynchronous execution on both kernels <test> & <test 1> . .	6
3	Integrator algorithm performance visualization	7
4	Reciprocal space offload scheme. Charge interpolation and Force interpolation are both written in a single kernel. They are naturally parallel except for the atomic contributions to the grid in the first one. The approach remains the same for data management between host and device as for real space: all data are by default device resident to prevent any sort of useless transfer. Regarding MPI communications, exchanges take place directly between GPUs through interconnection.	12
5	Illustration of compute balance due to the list reordering. Unbalanced computation in the first image induces an issue called warp discrepancy: a situation where all threads belonging to the same vector do not follow the same instructions. Minimizing that can increase kernel performance significantly since we ensure load balancing among each thread inside the vector.	13
6	Representation of cuFFT's communication recovering using device stream computation between direct and reciprocal space. Real space computation kernels are assigned to asynchronous stream 18. reciprocal ones goes into high priority asynchronous stream 17. real space kernel therefore recovers FFt grid exchanges. This profile was retrieved on 2GPUs	15
7	Performance ratio between single node GPU and single node CPU performance. Reference values can be found in [Table 1].	17

8	Profile of the matrix-vector compute kernel on the DHFR2 system. The left picture is obtained from the double precision run and the right one from simple precision. In both modes, results indicate an obvious latency issue coming from memory accessing pattern which prevents the device to reach its peak performance.	19
9	Reduction operation illustration on a 16 variables set. Each arithmetic operation generates an error ϵ_a that is accumulated during the sequential operation. On the other hand, parallel reduction uses intermediate variables to significantly reduce the error.	20
10	Absolute error between double precision implementation and mixed precision implementation on total potential energy. Forces root mean square deviation between DP and MP for systems from 648 up to 2 592 000 atoms. As expected, error on the energy grows linearly with the system size. Logarithmic regression gives 0.99 value for the curve slope. We reach 70 kcal/mol on the highest system. The relative energy for all systems is located under 1×10^{-5} . Regarding forces, the slight variations are due to the sensibility of the bonded forces to the conformation of the system: we can either obtain a slight growing error or an accurate RMSD like the 1 509 506 atoms test case. These numbers justify the use of Tinker-HP in mixed precision mode to perform accurate sampling.	23
11	Representation of interactions between two groups of atoms within Tinker-HP. $B_{size} = 8$ for the illustration	24

12	Illustration of a two dimensional Water Box partition along with groups. The left Figure shows a 64 cells partition of Ω while the right one refines this partitioning into 88 cells. Re-indexing all the atoms following the cells numbering and separating them equally shows all the groups. Here $B_{size} = 16$. A unique color is associated to every atom belonging to the same group. No cell contains more than B_{size} atoms or 2 groups. Once a group is selected -23-, searching for its neighboring groups is made through the set of cells (with respect to the periodic boundary condition) close to the cells it contains - 43 & 44 -. Once this set is acquired, all the group indexes greater or equal than the selected group constitute the actual list of neighbors to take the symmetry of the interactions into account. We see that the group's shape modulates the group neighborhood as illustrated with the right illustration and a spatially flat group 23.	26
13	Starting from the latest Figure 12, we represent the geometry resulting from the filtering process. As observed in comparison with the previous list, we significantly reduce group 23 neighborhood with the list filtering- From 144 atoms with the first list to 77 with the filtered one -. B_{comp} increases which corresponds to more interactions computed within each group pair.	29
14	Real space kernel profiling results in mixed precision using our new group-Atoms list.	30
15	Variation of the total energy during a NVE molecular dynamics simulation of the DHFR2 protein in both DP and mixed precision.	32
16	Single node mixed precision scalability on the Jean Zay Cluster (V100) using the AMOEBA polarizable force field	35
17	Two dimensional spatial decomposition of a simulation box with MPI distribution across 16 processes. ω_6 collects all the neighboring domains of ψ_6 . Here $n_b < n$	38

18	NVSHMEM memory distribution pattern across a four interconnected devices node. A symmetric reserved space is allocated by the NVSHMEM library at initialization. Thus, data is equally split across all devices in order. Every time a device needs to access data allocated with NVSHMEM, either a GMA or RMA is issued.	40
19	Performance and one node scalability results with the AMOEBA force field .	43

List of Tables

1	Single device benchmark : MD production per day (ns/day). All simulations were run using a RESPA/2 fs setup.	16
2	Single precision MD production (ns/day) within the OPENACC implementation	18
3	Available features in the initial Tinker- <i>HP</i> GPU release	33
4	Mixed precision performances assessed on single Geforce RTX-2080 Ti GPU card	36
5	Mixed precision performances assessed on single Quadro GV100 with RESPA Integrator at 2fs	36
6	Performance synthesis and scalability results on the Jean Zay (V100) and Selene (A100) machines. MD production in ns/day with the AMOEBA polarizable force field	42

References

- (1) Hollingsworth, S. A.; Dror, R. O. Molecular Dynamics Simulation for All. *Neuron* **2018**, *99*, 1129 – 1143.
- (2) Dror, R. O.; Dirks, R. M.; Grossman, J.; Xu, H.; Shaw, D. E. Biomolecular Simulation: A Computational Microscope for Molecular Biology. *Annual Review of Biophysics* **2012**, *41*, 429–452, PMID: 22577825.
- (3) Ponder, J. W.; Case, D. A. *Advances in protein chemistry*; Elsevier, 2003; Vol. 66; pp 27–85.
- (4) Huang, J.; Rauscher, S.; Nawrocki, G.; Ran, T.; Feig, M.; de Groot, B. L.; Grubmüller, H.; MacKerell, A. D. CHARMM36m: an improved force field for folded and intrinsically disordered proteins. *Nature methods* **2017**, *14*, 71–73.
- (5) Maier, J. A.; Martinez, C.; Kasavajhala, K.; Wickstrom, L.; Hauser, K. E.; Simmerling, C. ff14SB: Improving the Accuracy of Protein Side Chain and Backbone Parameters from ff99SB. *Journal of Chemical Theory and Computation* **2015**, *11*, 3696–3713, PMID: 26574453.
- (6) Jorgensen, W. L.; Maxwell, D. S.; Tirado-Rives, J. Development and Testing of the OPLS All-Atom Force Field on Conformational Energetics and Properties of Organic Liquids. *Journal of the American Chemical Society* **1996**, *118*, 11225–11236.
- (7) Oostenbrink, C.; Villa, A.; Mark, A. E.; Van Gunsteren, W. F. A biomolecular force field based on the free enthalpy of hydration and solvation: The GROMOS force-field parameter sets 53A5 and 53A6. *Journal of Computational Chemistry* **2004**, *25*, 1656–1676.
- (8) Shi, Y.; Ren, P.; Schnieders, M.; Piquemal, J.-P. *Reviews in Computational Chemistry* Volume 28; John Wiley and Sons, Ltd, 2015; Chapter 2, pp 51–86.

(9) Jing, Z.; Liu, C.; Cheng, S. Y.; Qi, R.; Walker, B. D.; Piquemal, J.-P.; Ren, P. Polarizable Force Fields for Biomolecular Simulations: Recent Advances and Applications. *Ann. Rev. Biophys.* **2019**, *48*, 371–394.

(10) Melcr, J.; Piquemal, J.-P. Accurate biomolecular simulations account for electronic polarization. *Front. Mol. Biosci.* **2019**, *6*, 143.

(11) Bedrov, D.; Piquemal, J.-P.; Borodin, O.; MacKerell, A. D.; Roux, B.; Schröder, C. Molecular Dynamics Simulations of Ionic Liquids and Electrolytes Using Polarizable Force Fields. *Chemical Reviews* **2019**, *119*, 7940–7995, PMID: 31141351.

(12) Lopes, P. E. M.; Huang, J.; Shim, J.; Luo, Y.; Li, H.; Roux, B.; MacKerell, A. D. Polarizable Force Field for Peptides and Proteins Based on the Classical Drude Oscillator. *Journal of Chemical Theory and Computation* **2013**, *9*, 5430–5449, PMID: 24459460.

(13) Lemkul, J. A.; Huang, J.; Roux, B.; MacKerell, A. D. An Empirical Polarizable Force Field Based on the Classical Drude Oscillator Model: Development History and Recent Applications. *Chemical Reviews* **2016**, *116*, 4983–5013, PMID: 26815602.

(14) Lin, F.-Y.; Huang, J.; Pandey, P.; Rupakheti, C.; Li, J.; Roux, B.; MacKerell, A. D. Further Optimization and Validation of the Classical Drude Polarizable Protein Force Field. *Journal of Chemical Theory and Computation* **2020**, *16*, 3221–3239, PMID: 32282198.

(15) Ren, P. Y.; Ponder, J. W. "Polarizable Atomic Multipole Water Model for Molecular Mechanics Simulation". *J. Phys. Chem.* **2003**, *107*, 5933–5947.

(16) Shi, Y.; Xia, Z.; Zhang, J.; Best, R.; Wu, C.; Ponder, J. W.; Ren, P. Polarizable Atomic Multipole-Based AMOEBA Force Field for Proteins. *J. Chem. Theory. Comput.* **2013**, *9*, 4046–4063.

(17) Zhang, C.; Lu, C.; Jing, Z.; Wu, C.; Piquemal, J.-P.; Ponder, J. W.; Ren, P. AMOEBA Polarizable Atomic Multipole Force Field for Nucleic Acids. *J. Chem. Theory. Comput.* **2018**, *14*, 2084–2108.

(18) Jiang, W.; Hardy, D. J.; Phillips, J. C.; MacKerell, A. D.; Schulten, K.; Roux, B. High-Performance Scalable Molecular Dynamics Simulations of a Polarizable Force Field Based on Classical Drude Oscillators in NAMD. *The Journal of Physical Chemistry Letters* **2011**, *2*, 87–92, PMID: 21572567.

(19) Lemkul, J. A.; Roux, B.; van der Spoel, D.; MacKerell Jr., A. D. Implementation of extended Lagrangian dynamics in GROMACS for polarizable simulations using the classical Drude oscillator model. *Journal of Computational Chemistry* **2015**, *36*, 1473–1479.

(20) Lagardère, L.; Jolly, L.-H.; Lipparini, F.; Aviat, F.; Stamm, B.; Jing, Z. F.; Harger, M.; Torabifard, H.; Cisneros, G. A.; Schnieders, M. J.; Gresh, N.; Maday, Y.; Ren, P. Y.; Ponder, J. W.; Piquemal, J.-P. Tinker-HP: a massively parallel molecular dynamics package for multiscale simulations of large complex systems with advanced point dipole polarizable force fields. *Chem. Sci.* **2018**, *9*, 956–972.

(21) Rackers, J. A.; Wang, Z.; Lu, C.; Laury, M. L.; Lagardère, L.; Schnieders, M. J.; Piquemal, J.-P.; Ren, P.; Ponder, J. W. Tinker 8: Software Tools for Molecular Design. *J. Chem. Theory and Comput.* **2018**, *14*, 5273–5289.

(22) Jolly, L.-H.; Duran, A.; Lagardère, L.; Ponder, J. W.; Ren, P.; Piquemal, J.-P. Raising the Performance of the Tinker-HP Molecular Modeling Package [Article v1.0]. *LiveCoMS*. **2019**, *1*, 10409.

(23) Stone, J. E.; Hardy, D. J.; Ufimtsev, I. S.; Schulten, K. GPU-accelerated molecular modeling coming of age. *Journal of Molecular Graphics and Modelling* **2010**, *29*, 116 – 125.

(24) Götz, A. W.; Williamson, M. J.; Xu, D.; Poole, D.; Le Grand, S.; Walker, R. C. Routine Microsecond Molecular Dynamics Simulations with AMBER on GPUs. 1. Generalized Born. *Journal of Chemical Theory and Computation* **2012**, *8*, 1542–1555, PMID: 22582031.

(25) Páll, S.; Zhmurov, A.; Bauer, P.; Abraham, M.; Lundborg, M.; Gray, A.; Hess, B.; Lindahl, E. Heterogeneous Parallelization and Acceleration of Molecular Dynamics Simulations in GROMACS. 2020.

(26) Salomon-Ferrer, R.; Götz, A. W.; Poole, D.; Le Grand, S.; Walker, R. C. Routine Microsecond Molecular Dynamics Simulations with AMBER on GPUs. 2. Explicit Solvent Particle Mesh Ewald. *Journal of Chemical Theory and Computation* **2013**, *9*, 3878–3888, PMID: 26592383.

(27) Eastman, P.; Swails, J.; Chodera, J. D.; McGibbon, R. T.; Zhao, Y.; Beauchamp, K. A.; Wang, L.-P.; Simmonett, A. C.; Harrigan, M. P.; Stern, C. D.; Wiewiora, R. P.; Brooks, B. R.; Pande, V. S. OpenMM 7: Rapid development of high performance algorithms for molecular dynamics. *PLOS Computational Biology* **2017**, *13*, 1–17.

(28) Harger, M.; Li, D.; Wang, Z.; Dalby, K.; Lagardère, L.; Piquemal, J.-P.; Ponder, J.; Ren, P. Tinker-OpenMM: Absolute and relative alchemical free energies using AMOEBA on GPUs. *Journal of Computational Chemistry* **2017**, *38*, 2047–2055.

(29) Potluri, S.; Luehr, N.; Sakharnykh, N. Simplifying Multi-GPU Communication with NVSHMEM. GPU Technology Conference. 2016.

(30) Frenkel, D.; Smit, B. *Understanding molecular simulation: from algorithms to applications*; Elsevier, 2001; Vol. 1.

(31) Lagardère, L.; Jolly, L. H.; Lipparini, F.; Aviat, F.; Stamm, B.; Jing, Z. F.; Harger, M.; Torabifard, H.; Cisneros, G. A.; Schnieders, M. J.; Gresh, N.; Maday, Y.; Ren, P. Y.;

Ponder, J. W.; Piquemal, J.-P. Tinker-HP: a massively parallel molecular dynamics package for multiscale simulations of large complex systems with advanced point dipole polarizable force fields. *Chem. Sci.* **2018**, *9*, 956–972.

(32) Wienke, S.; Springer, P.; Terboven, C.; an Mey, D. OpenACC — First Experiences with Real-World Applications. Euro-Par 2012 Parallel Processing. Berlin, Heidelberg, 2012; pp 859–870.

(33) Chandrasekaran, S.; Juckeland, G. *OpenACC for Programmers: Concepts and Strategies*, 1st ed.; Addison-Wesley Professional, 2017.

(34) Sanders, J.; Kandrot, E. *CUDA by example: an introduction to general-purpose GPU programming*; Addison-Wesley Professional, 2010.

(35) Volkov, V. Understanding Latency Hiding on GPUs. Ph.D. thesis, EECS Department, University of California, Berkeley, 2016.

(36) Kraus, J. An introduction to CUDA-aware MPI. *Weblog entry]. PARALLEL FORALL 2013*,

(37) Essmann, U.; Perera, L.; Berkowitz, M. L.; Darden, T.; Lee, H.; Pedersen, L. G. A smooth particle mesh Ewald method. *The Journal of Chemical Physics* **1995**, *103*, 8577–8593.

(38) Lagardère, L.; Lipparini, F.; Polack, E.; Stamm, B.; Cancès, E.; Schnieders, M.; Ren, P.; Maday, Y.; Piquemal, J.-P. Scalable Evaluation of Polarization Energy and Associated Forces in Polarizable Molecular Dynamics: II. Toward Massively Parallel Computations Using Smooth Particle Mesh Ewald. *Journal of Chemical Theory and Computation* **2015**, *11*, 2589–2599, PMID: 26575557.

(39) NVIDIA Corporation, CUDA Toolkit 11.1 CUFFT Library Programming Guide 2020 ,<http://developer.nvidia.com/nvidia-gpu-computing-documentation>. 2020.

(40) Lipparini, F.; Lagardère, L.; Stamm, B.; Cancès, E.; Schnieders, M.; Ren, P.; Marday, Y.; Piquemal, J.-P. Scalable Evaluation of Polarization Energy and Associated Forces in Polarizable Molecular Dynamics: I. Toward Massively Parallel Direct Space Computations. *Journal of Chemical Theory and Computation* **2014**, *10*, 1638–1651, PMID: 26512230.

(41) Phillips, J. C.; Gengbin Zheng,; Kumar, S.; Kale, L. V. NAMD: Biomolecular Simulation on Thousands of Processors. SC '02: Proceedings of the 2002 ACM/IEEE Conference on Supercomputing. 2002; pp 36–36.

(42) Tuckerman, M.; Berne, B. J.; Martyna, G. J. Reversible multiple time scale molecular dynamics. *J. Chem. Phys.* **1992**, *97*, 1990–2001.

(43) Bussi, G.; Donadio, D.; Parrinello, M. Canonical sampling through velocity rescaling. *J. Chem. Phys.* **2007**, *126*, 014101.

(44) Zhou, J.; Ross, K. A. Implementing database operations using SIMD instructions. Proceedings of the 2002 ACM SIGMOD international conference on Management of data. 2002; pp 145–156.

(45) Le Grand, S.; Götz, A. W.; Walker, R. C. SPFP: Speed without compromise—A mixed precision model for GPU accelerated molecular dynamics simulations. *Computer Physics Communications* **2013**, *184*, 374 – 380.

(46) Bowers, K. J.; Dror, R. O.; Shaw, D. E. The midpoint method for parallelization of particle simulations. *The Journal of Chemical Physics* **2006**, *124*, 184109.

(47) Lagardère, L.; Aviat, F.; Piquemal, J.-P. Pushing the Limits of Multiple-Time-Step Strategies for Polarizable Point Dipole Molecular Dynamics. *The Journal of Physical Chemistry Letters* **2019**, *10*, 2593–2599.

(48) Célerse, F.; Lagardère, L.; Derat, E.; Piquemal, J.-P. Massively parallel implementation of Steered Molecular Dynamics in Tinker-HP:comparisons of polarizable and non-polarizable simulations of realistic systems. *J. Chem. Theory. Comput.* **2019**, *15*, 3694–3709.

(49) Miao, Y.; Feher, V. A.; McCammon, J. A. Gaussian accelerated molecular dynamics: Unconstrained enhanced sampling and free energy calculation. *Journal of chemical theory and computation* **2015**, *11*, 3584–3595.

(50) Jorgensen, W. L.; Maxwell, D. S.; Tirado-Rives, J. "Development and Testing of the OPLS All-Atom Force Field on Conformational Energetics and Properties of Organic Liquids". *J. Am. Chem. Soc.* **1996**, *117*, 11225–11236.

(51) Inizan, T. J.; Célerse, F.; Adjoua, O.; Ahdab, D. E.; Jolly, L.-H.; Liu, C.; Ren, P.; Montes, M.; Lagarde, N.; Lagardère, L.; Monmarché, P.; Piquemal, J.-P. High-Resolution Mining of SARS-CoV-2 Main Protease Conformational Space: Supercomputer-Driven Unsupervised Adaptive Sampling, 10.26434/chemrxiv.13003166.v1. **2020**,

(52) Chapman, B.; Curtis, T.; Pophale, S.; Poole, S.; Kuehn, J.; Koelbel, C.; Smith, L. Introducing OpenSHMEM: SHMEM for the PGAS community. Proceedings of the Fourth Conference on Partitioned Global Address Space Programming Model. 2010; pp 1–3.

(53) Liu, C.; Piquemal, J.-P.; Ren, P. AMOEBA+ Classical Potential for Modeling Molecular Interactions. *Journal of Chemical Theory and Computation* **2019**, *15*, 4122–4139, PMID: 31136175.

(54) Liu, C.; Piquemal, J.-P.; Ren, P. Implementation of Geometry-Dependent Charge Flux into the Polarizable AMOEBA+ Potential. *The Journal of Physical Chemistry Letters* **2020**, *11*, 419–426, PMID: 31865706.

(55) Gresh, N.; Cisneros, G. A.; Darden, T. A.; Piquemal, J.-P. *Journal of Chemical Theory and Computation* **2007**, 3, 1960–1986, PMID: 18978934.